

FIXED POINT ANALYSIS OF DOUGLAS-RACHFORD SPLITTING FOR PTYCHOGRAPHY AND PHASE RETRIEVAL

ALBERT FANNJIANG AND ZHEQING ZHANG

ABSTRACT. Douglas-Rachford Splitting (DRS) methods based on the proximal point algorithms for the Poisson and Gaussian log-likelihood functions are proposed for ptychography and phase retrieval.

Fixed point analysis shows that the DRS iterated sequences are always bounded explicitly in terms of the step size and that the fixed points are linearly stable if and only if the fixed points are regular solutions. This alleviates two major drawbacks of the classical Douglas-Rachford (CDR) algorithm: slow convergence when the feasibility problem is consistent and divergent behavior when the feasibility problem is inconsistent.

Moreover, the fixed point analysis decisively leads to the selection of an optimal step size which in turn renders the Gaussian DRS method in a particularly simple form with no tuning parameter (Averaged Projection-Reflection). When applied to the challenging problem of *blind* ptychography, which seeks to recover both the object and the probe simultaneously, the DRS methods converge geometrically and globally when properly initialized.

1. INTRODUCTION

Phase retrieval may be posed as an inverse problem in which an object vector with certain properties is to be reconstructed from the intensities of its Fourier transform. By encoding the properties and the Fourier intensities as constraint sets, phase retrieval can be cast as a feasibility problem, i.e. the problem of finding a point in the intersection of the constraint sets. The challenge is that the intensities of the Fourier transform results in a non-convex constraint set (a high dimensional torus of variable radii).

Projection algorithms comprise a general class of iterative methods for solving feasibility problems by projecting onto each of the constraint sets at each step [5]. The most basic projection algorithm is von Neumann's Alternating Projection (AP) (aka Error Reduction in phase retrieval [21]). However, AP tends to stagnate when applied to phase retrieval, resulting in poor performance.

A better method than AP is the classical Douglas-Rachford (CDR) algorithm [12, 22, 22, 30], which apparently can avoid the stagnation problem in many non-convex problems. When applied to phase retrieval, CDR is a special case of Fienup's Hybrid-Input-Output algorithm [1, 21].

In addition to the standard phase retrieval, CDR has been applied to ptychography under the name of difference map [42, 43, 46]. Ptychography uses a localized coherent probe to illuminate different parts of a unknown extended object and collect multiple diffraction patterns as measurement data (Figure 1). The redundant information in the overlap between adjacent illuminated spots is then exploited to improve phase retrieval methods [36, 39]. Recently

ptychography has been extended to the Fourier domain [37, 49]. In Fourier ptychography, illumination angles are scanned sequentially with a programmable array source with the diffraction pattern measured at each angle [28, 45]. Tilted illumination samples different regions of Fourier space, as in synthetic-aperture and structured-illumination imaging.

Local, linear convergence of CDR as applied to phase retrieval as well as ptychography was recently proved in [8, 9]. Conditions for global convergence, however, are not known. Numerical evidence points to sub-linear rate when convergence happens. On the other hand, for inconsistent feasibility problems, CDR iteration is known to diverge to infinity even in the convex case (see Proposition 2.1(ii)). This poses a great challenge to CDR when the data contain noise because in phase retrieval the dimension of the measurement data is much higher than that of the unknown object (an over-determined system).

The purpose of this work is to develop reconstruction schemes based on more general Douglas-Rachford splitting (DRS) with adjustable step sizes, perform the fixed point analysis and demonstrate numerical convergence. CDR is the limiting case of DRS.

The DRS method is an optimization method based on proximal operators, a natural extension of projections, and is closely related to the Alternating Direction Method of Multipliers (ADMM). The performance of DRS and ADMM in the non-convex setting depends sensitively on the choice of the objective functions as well as the step sizes. Typically, global convergence of DRS requires an objective function possessing a uniformly Lipschitz gradient and sufficiently large step sizes [8, 26, 29], both of which, however, tend to hinder the performance of DRS.

In this paper, the objective function is based on the log-likelihood function for the most important Poisson noise, which does not have a uniformly Lipschitz gradient, with an optimal step size, which is necessarily quite large.

We show by a fixed point analysis that the DRS method is well behaved in the sense that the DRS iterated sequences are always bounded (explicitly in terms of the step size) and that the fixed points are linearly stable if and only if the fixed points are regular solutions. In other words, the DRS methods remove CDR's two major drawbacks: slow convergence when the feasibility problem is consistent and divergent behavior when the feasibility problem is inconsistent.

Moreover, the fixed point analysis leads to the determination of the optimal step size and, along with it, simple and efficient algorithms with no tuning parameter (Averaged Projection-Reflection). The main application considered is the more challenging form of ptychography called *blind ptychography* which seeks to recover both the unknown object and the probe function simultaneously. When properly initialized, the DRS algorithms with the optimal step size converge globally and geometrically to the true solution modulo the inherent ambiguities.

The rest of the paper is organized as follows. In Section 3, we introduce the Douglas-Rachford splitting method as the key ingredient of our reconstruction algorithms, Gaussian-DRS and Poisson-DRS. We give the fixed point and stability analysis in Sections 4, 5 and 6. In Section 7, we discuss the selection of the optimal step size. In Section 8, we discuss the application to blind ptychography and in Section 9, we present numerical experiments. In Appendix A, we

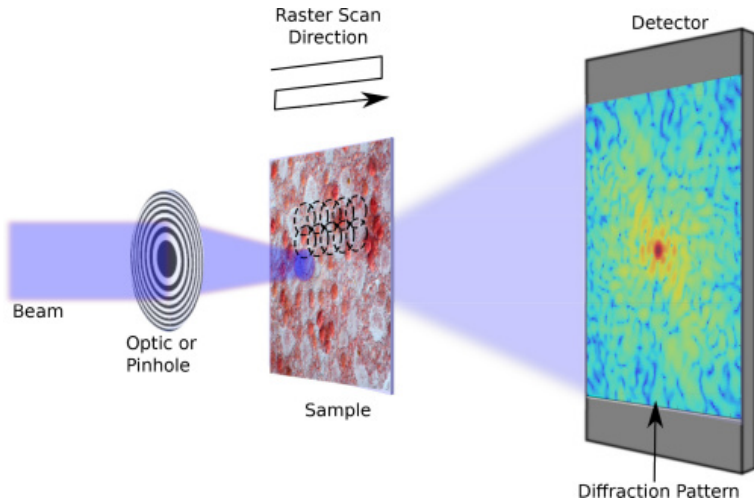


FIGURE 1. Simplified ptychographic setup showing a Cartesian grid used for the overlapping raster scan positions [35]. See Appendix A for details.

discuss the structure of the measurement matrices. In Appendix B, we show that Gaussian-DRS is an asymptotic form of Poisson-DRS. In Appendix C we give a perturbation analysis for the Poisson DRS. In Appendix D, we analyze the eigenstructure of the measurement matrices. We conclude in Section 10. A preliminary version of the present work is given in [18].

2. CLASSICAL DOUGLAS-RACHFORD (CDR)

CDR is based on the following characterization of *convex* feasibility problems.

Let X and Y be the constraint sets. Let P_X be the projection onto X and $R_X = 2P_X - I$ the corresponding reflector. P_Y and R_Y are defined likewise. Then

$$(1) \quad u \in X \cap Y \quad \text{if and only if} \quad u = R_Y R_X u$$

[23]. The latter fixed point equation motivates the Peaceman-Rachford (PR) method: For $k = 0, 1, 2, \dots$

$$u_{k+1} = R_Y R_X u_k.$$

CDR is the *averaged* version of PR: For $k = 0, 1, 2, \dots$

$$(2) \quad u_{k+1} = \frac{1}{2}u_k + \frac{1}{2}R_Y R_X u_k.$$

As a result, CDR is sometimes called the *Averaged Alternating Reflections* (AAR).

A standard result for CDR in the convex case is this.

Proposition 2.1. [3] *Suppose X and Y are closed and convex sets of a finite-dimensional vector space E . For any $u_0 \in E$, one of the following alternatives holds:*

- (i) $X \cap Y \neq \emptyset$ and (u_n) converges to a point u such that $P_X u \in X \cap Y$;
- (ii) $X \cap Y = \emptyset$ and $\|u_n\| \rightarrow \infty$.

In alternative (i), the limit point u is a fixed point of the CDR map (2), which is necessarily in $X \cap Y$; in alternative (ii) the feasibility problem is inconsistent, resulting in divergent CDR iterated sequences, a major drawback of CDR.

The CDR map (2) is often written in the following form

$$u_{k+1} = u_k + P_Y R_X u_k - P_X u_k$$

which is equivalent to the 3-step iteration

$$\begin{aligned} (3) \quad & y_k = P_X u_k; \\ (4) \quad & z_k = P_Y(2y_k - u_k) = P_Y R_X u_k \\ (5) \quad & u_{k+1} = u_k + z_k - y_k \end{aligned}$$

2.1. Phase retrieval as feasibility. For any finite dimensional vector u , define its modulus vector $|u|$ as $|u|[j] = |u[j]|$ and its phase vector $\text{sgn}(u)$ as

$$\text{sgn}(u)[j] = \begin{cases} 1 & \text{if } u[j] = 0 \\ u[j]/|u[j]| & \text{else.} \end{cases}$$

where j is the index for the vector component.

In phase retrieval including ptychography, we can write the given data b as

$$(6) \quad b = |u| \quad \text{with} \quad u = Af$$

for some measurement matrix A and unknown object f . For phase retrieval and ptychography, A has some special features described in Appendix A. For most of the subsequent analysis, however, these special features are not relevant.

Let O be the object space, typically a finite-dimensional complex vector space, and $X = AO$. Since the object is a two dimensional, complex-valued image, we let $O = \mathbb{C}^{n^2}$ where n is the number of pixels in each dimension.

Let N be the total number of data. The data manifold

$$Y := \{u \in \mathbb{C}^N : |u| = b\}$$

is a N (real) dimensional torus. For phase retrieval it is necessary that $N > 2n^2$. Without loss of generality we assume that A has a full rank.

The problem of phase retrieval and ptychography can be formulated as the feasibility problem

$$(7) \quad \text{Find } u \in X \cap Y,$$

in the transform domain instead of the object domain.

Let us clarify the meaning of solution in the transform domain since A is overdetermining. Let \odot denotes the component-wise (Hadamard) product and we can write

$$(8) \quad \begin{aligned} P_X u &= AA^\dagger u, & P_Y u &= b \odot \text{sgn}(u) \\ R_X &= 2P_X - I, & R_Y &= 2P_Y - I. \end{aligned}$$

We refer to $u = e^{i\alpha}Af, \alpha \in \mathbb{R}$, as the *true* solution (in the transform domain), up to a constant phase factor $e^{i\alpha}$. We say that u is a *generalized solution* (in the transform domain) if

$$|\hat{u}| = b, \quad \hat{u} := P_X u.$$

Accordingly, the alternative (i) in Proposition 2.1 means that if a convex feasibility problem is consistent then every CDR iterated sequence converges to a generalized solution and hence every fixed point is a generalized solution.

Typically a generalized solution u is neither a feasible solution (since $|u|$ may not equal b) nor unique (since A is overdetermining) and $u + z$ is also a generalized solution if $P_X z = 0$. We call u a *regular* solution if u is a generalized solution and $P_X u = u$.

Let $\hat{u} = P_X u$ for a generalized solution u . Since $P_X \hat{u} = \hat{u}$ and $|\hat{u}| = b$, \hat{u} is a regular solution. Let us state this simple fact for easy reference.

Proposition 2.2. *If u is a generalized solution, then $P_X u$ is a regular solution.*

The goal of the inverse problem (6) is the unique determination of f , up to a constant phase factor, from the given data b . In other words, uniqueness holds if, and only if, all regular solutions \hat{u} have the form

$$(9) \quad \hat{u} = e^{i\alpha}Af$$

or equivalently, any generalized solution u is an element of the $(2N - 2n^2)$ real-dimensional vector space

$$(10) \quad \{e^{i\alpha}Af + z : P_X z = 0, z \in \mathbb{C}^N, \alpha \in \mathbb{R}\}.$$

In the transform domain, the uniqueness is characterized by the uniqueness of the regular solution, up to a constant phase factor. Geometrically, uniqueness means that the intersection $X \cap Y$ is a circle (parametrized $e^{i\alpha}$ times Af).

As proved in [8], when the uniqueness (10) holds, the fixed point set of the CDR map (2) is exactly the continuum set

$$(11) \quad \{u = e^{i\alpha}Af + z : P_X z = 0, \text{sgn}(u) = \alpha + \text{sgn}(Af), z \in \mathbb{C}^N, \alpha \in \mathbb{R}\}.$$

In (11), the phase relation $\text{sgn}(u) = \alpha + \text{sgn}(Af)$ implies that $z = \eta \odot \text{sgn}(u), \eta \in \mathbb{R}^N, b + \eta \geq 0$. So the set (11) can be written as

$$(12) \quad \{e^{i\alpha}(b + \eta) \odot \text{sgn}(Af) : P_X(\eta \odot \text{sgn}(Af)) = 0, b + \eta \geq 0, \eta \in \mathbb{R}^N, \alpha \in \mathbb{R}\},$$

which is a $(N - 2n^2)$ real-dimensional set, a much larger set than the circle $\{e^{i\alpha}Af : \alpha \in \mathbb{R}\}$. On the other hand, the fixed point set (11) is N -dimension lower than the set (10) of generalized solutions.

However, the boundary of the fixed point set (12) are degenerate in the sense that they have vanishing components, i.e. $(b + \eta)[j] = 0$ for some j . Empirical evidence shows that degenerate fixed points can slow down convergence. As a result, even though the CDR map is geometrically convergent in the vicinity of the true solution, numerical evidence suggests that globally (starting with a random initial guess) the CDR map converges sub-linearly [8].

3. DOUGLAS-RACHFORD SPLITTING (DRS)

Douglas-Rachford Splitting (DRS) is an optimization method for solving the following minimization problem:

$$(13) \quad \min_u K(u) + L(u)$$

where the objective functions L and K represent the data constraint Y and the object constraint X , respectively.

To deal with the divergence behavior of CDR (Proposition 2.1 (ii)) in the case of, e.g. noisy data, we consider the Poisson log-likelihood cost functions [4, 44]

$$(14) \quad \text{Poisson: } L(u) = \sum_i |u[i]|^2 - b^2[i] \ln |u[i]|^2$$

based on the maximum likelihood principle for the Poisson noise model. The Poisson noise is the most prevalent noise in X-ray coherent diffraction. The Poisson log-likelihood function (14) is asymptotically reducible to

$$(15) \quad \text{Gaussian: } L(u) = \frac{1}{2} \| |u| - b \|^2$$

as shown in Appendix B. The maximum likelihood scheme is a variance stabilization scheme which uniformizes the probability distribution for every pixel regardless of the measured intensity value [27]. See [25, 48] for more choices of objective functions.

The amplitude-based Gaussian objective function (15) is well known to outperform the intensity-based objective function $\frac{1}{2} \| |u|^2 - b^2 \|^2$, even though the latter is more smooth [47]. Due to the non-differentiability of both K and L , the global convergence property of the proposed DRS method is beyond the current framework of analysis [29]. The ptychographic iterative engines, PIE [19, 20, 40], ePIE [33] and rPIE [31], are also related to the mini-batch gradient method for the amplitude-based cost function (15).

For K , we let $K(u)$ be the indicator function of the range of A , i.e. a “hard” constraint.

When the corresponding feasibility problem is consistent (feasible), there exist $u \in \mathbb{C}^N$ such that $|u| = b$ and $u = Ag$ for some $g \in \mathbb{C}^{n^2}$, which are exactly the global minimizers of (13), realizing the minimum value 0, as well as the regular solutions defined in Section 2.1.

When the corresponding feasibility problem is inconsistent (infeasible), the minimum value of (13) is unknown and the global minimizers are harder to characterize.

DRS is based on the proximal operator which is a generalization of projection. The proximal point relative to a function G is given by

$$\text{prox}_G(u) := \underset{x}{\operatorname{argmin}} G(x) + \frac{1}{2} \|x - u\|^2.$$

With the objective functions (14) or (15), P_X is replaced by $P_{K/\rho}$ and P_Y by $P_{L/\rho}$, respectively, with the step size $\gamma = 1/\rho$. The 3-step procedure (3)-(5) is replaced by

$$(16) \quad v_l = \text{prox}_{K/\rho}(u_l);$$

$$(17) \quad w_l = \text{prox}_{L/\rho}(2v_l - u_l)$$

$$(18) \quad u_{l+1} = u_l + w_l - v_l$$

for $l = 1, 2, 3 \dots$.

For convex optimization, DRS (16)-(18) is equivalent to the Alternating Direction Method of Multipliers (ADMM) applied to the dual problem to (13).

For our choice of K , $\text{prox}_{K/\rho}(u) = P_X u = AA^\dagger u$ is independent of ρ . This should be contrasted with the choice of the more smooth distance function adopted in [29] for the tractability of convergence analysis.

If we define the reflector \mathcal{R}_Y corresponding to $\text{prox}_{L/\rho}(u)$ as

$$(19) \quad \mathcal{R}_Y u := 2 \text{prox}_{L/\rho}(u) - u,$$

then we can write the system (16)-(18) as

$$(20) \quad u_{k+1} = \frac{1}{2}u_k + \frac{1}{2}\mathcal{R}_Y R_X u_k$$

which is equivalent to

$$(21) \quad x_{k+1} = \frac{1}{2}x_k + \frac{1}{2}R_X \mathcal{R}_Y x_k$$

in terms of $x_k := R_X u_k$. In other words, the order of carrying out $\text{prox}_{L/\rho}$ and $\text{prox}_{K/\rho}$ does not matter in the current DRS set-up.

For the Gaussian objective function (15), the proximal point can be explicitly derived

$$\begin{aligned} \text{prox}_{L/\rho}(u) &= \frac{1}{\rho+1}b \odot \text{sgn}(u) + \frac{\rho}{\rho+1}u \\ &= \frac{1}{\rho+1}(b + \rho|u|) \odot \text{sgn}(u), \end{aligned}$$

an averaged projection with the relaxation parameter ρ . Thus the Gaussian-DRS map is given by

$$(22) \quad u_{k+1} = \frac{1}{2}u_k + \frac{\rho-1}{2(\rho+1)}x_k + \frac{1}{\rho+1}b \odot \text{sgn}(x_k), \quad x_k := R_X u_k$$

which may be written as

$$u_{k+1} = \frac{1}{2}u_k + \frac{\rho}{2(\rho+1)}R_X u_k + \frac{1}{2(\rho+1)}R_Y R_X u_k$$

for ease of comparison with the CDR map (2).

For the Poisson case (14), the DRS map had a more complicated form

$$(23) \quad u_{k+1} = \frac{1}{2}u_k - \frac{1}{\rho+2}R_X u_k + \frac{\rho}{2(\rho+2)} \left[|R_X u_k|^2 + \frac{8(2+\rho)}{\rho^2}b^2 \right]^{1/2} \odot \text{sgn}(R_X u_k)$$

where b^2 is the vector with component $b^2[j] = (b[j])^2$ for all j .

After the iteration is terminated with the terminal vector u_* , the object estimate is obtained by

$$(24) \quad f_* = A^\dagger u_*.$$

We shall refer to DRS with the Poisson log-likelihood function (23) and the Gaussian version (22) by the acronyms *Poisson-DRS* and *Gaussian-DRS*, respectively. The computation involved in Gaussian-DRS and Poisson-DRS are mostly pixel-wise operations (hence efficient) except for the pseudoinverses $A^\dagger = (A^*A)^{-1}A^*$. For phase retrieval including ptychography, we can write $A = \Psi D$ where Ψ is an isometry (related to the discrete Fourier transform) and D is a positive, diagonal matrix (related to normalization) and hence $A^\dagger = D^{-1}\Psi^* = D^{-2}A^*$, which is easy to compute numerically (see Appendix A). In the limiting case of $\rho = 0$, both Gaussian-DRS and Poisson-DRS become the CDR algorithm.

4. FIXED POINTS

For simplicity of presentation, we shall focus on the case of the Gaussian DRS.

Let Γ denote the mapping defined by the right hand side of (22). By definition, all fixed points u satisfy the equation

$$(25) \quad u = \Gamma(u)$$

and hence after some algebra by (22)

$$(26) \quad P_X u + \rho P_X^\perp u = b \odot \text{sgn}(R_X u).$$

The main result of this section is that the iteration of Γ always produces a sequence bounded in norm by

$$\frac{\|b\|}{\min\{\rho, 1\}} \quad \text{for } \rho > 0$$

(Theorem 4.6) with slightly better bounds on the fixed points (Corollary 4.9). Therefore, Gaussian-DRS is free of the divergence problem associated with CDR in the infeasible case.

It is often convenient to perform the analysis in terms of the pair of variables u and $x := R_X u$. Here are some basic relations between u and x .

Proposition 4.1. *For any $u \in \mathbb{C}^N$, $x := R_X u$ satisfies*

$$u = R_X x, \quad P_X u = P_X x, \quad P_X^\perp u = -P_X^\perp x.$$

Proof. First note that

$$R_X x = 2P_X x - x = 2P_X u - (2P_X u - u) = u.$$

Moreover,

$$P_X x = P_X R_X u = P_X (2P_X u - u) = 2P_X u - P_X u = P_X u.$$

and

$$P_X^\perp x = x - P_X x = 2P_X u - u - P_X x = 2P_X u - u - P_X u = P_X u - u = -P_X^\perp u.$$

□

Proposition 4.2. *Any $u \in \mathbb{C}^N$ is a generalized solution if and only if $x := R_X u$ is a generalized solution.*

Proof. If u is a generalized solution, then $P_X u = P_X x$ by Proposition 4.1. Now that x is a generalized solution, the converse is also true by the same argument.

□

Proposition 4.3. *If u is a generalized solution, then $P_X u$ is a regular solution and a fixed point.*

Proof. Let $\hat{u} = P_X u$. By Proposition 2.2 \hat{u} is a regular solution. Moreover $\Gamma(u)$ becomes

$$\frac{1}{2}\hat{u} + \frac{\rho-1}{2(\rho+1)}\hat{u} + \frac{1}{\rho+1}b \odot \text{sgn}(\hat{u}) = \frac{1}{2}\hat{u} + \frac{\rho-1}{2(\rho+1)}\hat{u} + \frac{1}{\rho+1}\hat{u}$$

which equals \hat{u} . Therefore \hat{u} is a fixed point.

□

Proposition 4.4. *Suppose $P_X u = u$. Then u is a regular solution if, and only if, u is a fixed point.*

Proof. Under the assumption $P_X u = u$, $u = R_X u$ and $\Gamma(u)$ becomes

$$(27) \quad \frac{1}{2}u + \frac{\rho-1}{2(\rho+1)}u + \frac{1}{\rho+1}b \odot \text{sgn}(u) = \frac{\rho}{1+\rho}u + \frac{1}{\rho+1}b \odot \text{sgn}(u).$$

Therefore, if u is a fixed point, then (26) implies

$$u = b \odot \text{sgn}(u)$$

and hence $|u| = b$, i.e. u is a regular solution.

On the other hand, if $|u| = b$, then the right hand side of (27) becomes

$$\frac{\rho}{1+\rho}u + \frac{1}{\rho+1}b \odot \text{sgn}(u) = \frac{\rho}{1+\rho}u + \frac{1}{\rho+1}u = u$$

implying that u is a fixed point.

□

Writing

$$I = P_X + P_X^\perp \quad \text{and} \quad R_X = P_X - P_X^\perp,$$

and using Proposition 4.1 we can put the Gaussian DRS map and the fixed point equation in the following forms.

Proposition 4.5. *The Gaussian DRS iteration (22) is equivalent to*

$$(28) \quad P_X u_{k+1} = \frac{\rho}{\rho+1} P_X u_k + \frac{1}{\rho+1} P_X P_Y x_k$$

$$(29) \quad P_X^\perp u_{k+1} = \frac{1}{\rho+1} P_X^\perp u_k + \frac{1}{\rho+1} P_X^\perp P_Y x_k$$

where $x_k := R_X u_k$. Therefore any fixed point u satisfies

$$(30) \quad P_X x = P_X P_Y x$$

$$(31) \quad -\rho P_X^\perp x = P_X^\perp P_Y x,$$

where $x := R_X u$, or equivalently

$$(32) \quad P_X x - \rho P_X^\perp x = b \odot \text{sgn}(x)$$

$$(33) \quad P_X x + \rho P_X^\perp x = R_X (b \odot \text{sgn}(x)).$$

Next we show that the Gaussian DRS map Γ with $\rho > 0$ always produces a bounded iterated sequence, in contrast to the divergence behavior of CDR given in Proposition 2.1 (ii).

Theorem 4.6. *Suppose that P_X is an orthogonal projection. Let $u_{k+1} := \Gamma(u_k)$, $k \in \mathbb{N}$, and $x_k := R_X u_k$. Then, for $\rho > 0$, $\{u_k\}$ and $\{x_k\}$ are bounded iterated sequences. Moreover,*

$$(34) \quad \limsup_{k \rightarrow \infty} \|u_k\| = \limsup_{k \rightarrow \infty} \|x_k\| \leq \frac{\|b\|}{\min\{\rho, 1\}} \quad \text{for } \rho > 0$$

and hence all fixed points u satisfy

$$(35) \quad \|u\| \leq \frac{\|b\|}{\min\{\rho, 1\}} \quad \text{for } \rho > 0.$$

Remark 4.7. *As remarked below (24) (see Appendix A), $A^\dagger = D^{-2} A^*$ with a diagonal matrix D in phase retrieval and ptychography. Consequently, $P_X = A A^\dagger$ is Hermitian-symmetric and hence an orthogonal projection.*

Remark 4.8. *The upper bounds (34) is consistent with Proposition 2.1 (ii) and the numerical evidence that the DRS iterations tend to wander in a greater range with $\rho < 1$.*

Proof. Since P_X is an orthogonal projection, we have

$$\|x_k\| = \|u_k\| = \sqrt{\|P_X x_k\|^2 + \|P_X^\perp x_k\|^2}.$$

By Proposition 4.5 we then have the estimates

$$(36) \quad \begin{aligned} \|u_{k+1}\| &\leq \left\| \frac{1}{\rho+1} P_X^\perp u_k + \frac{\rho}{\rho+1} P_X u_k \right\| + \frac{1}{\rho+1} \|P_Y x_k\| \\ &= \left[\frac{1}{(\rho+1)^2} \|P_X^\perp u_k\|^2 + \frac{\rho^2}{(\rho+1)^2} \|P_X u_k\|^2 \right]^{1/2} + \frac{1}{\rho+1} \|P_Y x_k\| \\ &\leq \frac{\max\{\rho, 1\}}{\rho+1} \|u_k\| + \frac{1}{\rho+1} \|b\|. \end{aligned}$$

Hence, iterating (36) for $\rho \geq 1$ we obtain

$$\|u_{k+1}\| \leq \frac{\rho^k}{(\rho+1)^k} \|u_1\| + \frac{\|b\|}{\rho+1} \sum_{j=0}^{k-1} \frac{\rho^j}{(1+\rho)^j}$$

and, after passing to the limit, the upper bound (34).

On the other hand, for $\rho < 1$,

$$\|u_{k+1}\| \leq \frac{1}{(\rho+1)^k} \|u_1\| + \|b\| \sum_{j=1}^k \frac{1}{(\rho+1)^j}$$

implying (34). □

We can improve (35) slightly by Proposition 4.5.

Corollary 4.9. *Suppose P_X is an orthogonal projection. For any fixed point u , let $x := R_X u$. Then*

$$(37) \quad \|u\| = \|x\| < \|b\| \quad \text{if } \rho > 1$$

and

$$(38) \quad \|b\| < \|u\| = \|x\| \leq \|b\|/\rho \quad \text{if } \rho \in (0, 1)$$

unless $P_X x = x$ (or equivalently $P_X u = u$), in which case $u = x$ is a regular solution.

On the other hand, for $\rho = 1$, $\|u\| = \|x\| = \|b\|$ for any fixed point u .

Proof. By (32) and that P_X is an orthogonal projection, we have

$$(39) \quad \|P_X x\|^2 + \rho \|P_X^\perp x\|^2 = \|b\|^2$$

which implies

$$(40) \quad \|u\| = \|x\| \begin{cases} < \|b\| & \text{for } \rho > 1 \\ > \|b\| & \text{for } \rho < 1 \end{cases} \quad \text{if } \|P_X^\perp x\| \neq 0.$$

If $\|P_X^\perp x\| = 0$, then $x = P_X x$ and (32) becomes $x = b \odot \text{sgn}(x)$, implying $|x| = b$. Likewise, $x = P_X x$ implies that $u = x$.

Moreover, by (35), $\|u\| = \|x\| \leq \|b\|/\rho$ for $\rho \in (0, 1)$. Hence (40) can be further strengthened to the statement (37)-(38).

For $\rho = 1$, (39) implies that $\|x\| = \|b\|$. □

In Appendix C we give a perturbation analysis for the similar result in the Poisson case with small ρ .

5. STABILITY ANALYSIS

When the uniqueness (10) holds, the fixed point set of CDR ($\rho = 0$) is explicitly given in (11). For $\rho > 0$, the fixed point set is much harder to characterize explicitly. Instead, we show that the desirable fixed points (i.e. regular solutions) are automatically distinguished from the other non-solutional fixed points by the stability type.

Roughly speaking, we shall prove that for $\rho \geq 1$ all linearly stable fixed points must be regular solutions (Theorem 5.2) and that for $\rho \geq 0$ all regular solutions are linearly stable (Theorem 5.3). In other words, for $\rho \geq 1$, we need not concern with the problem of stagnation near a fixed point that is not a regular solution (a common problem with AP). Moreover, we know that the regular solutions are strictly attractive under additional mild conditions (Corollary 6.2). On the other hand, the problem of divergence (associated with CDR) when the data constraint is infeasible does not arise for Gaussian-DRS in view of Theorem 4.6.

Proposition 5.1. *Let $x := R_X u$ and assume $|x| > 0$. Set*

$$(41) \quad \Omega = \text{diag}(\text{sgn}(x)), \quad \tilde{P}_X = \Omega^* P_X \Omega, \quad \tilde{R}_X = \Omega^* R_X \Omega.$$

Then

$$\lim_{\epsilon \rightarrow 0} \Omega^* (\Gamma(u + \epsilon v) - \Gamma(u)) / \epsilon = J_A(\eta), \quad \eta = \Omega^* v$$

where

$$(42) \quad J_A(\eta) = \frac{1}{2} \eta + \frac{\rho - 1}{2(\rho + 1)} \tilde{R}_X \eta + \frac{\iota}{\rho + 1} \frac{b}{|x|} \odot \Im \left[\tilde{R}_X \eta \right].$$

Proof. The key observation is that the derivative of $\text{sgn}(c) = c/|c| \in \mathbb{C}, c \neq 0$, is given by

$$\begin{aligned} \lim_{\epsilon \rightarrow 0} \frac{1}{\epsilon} \left[\frac{c + \epsilon a}{|c + \epsilon a|} - \frac{c}{|c|} \right] &= \lim_{\epsilon \rightarrow 0} \frac{\text{sgn}(c)}{\epsilon} \left[\frac{1 + \epsilon a/c}{|1 + \epsilon a/c|} - 1 \right] \\ &= \iota \Im \left[\frac{a}{c} \right] \text{sgn}(c) \\ &= \iota \Im [\text{sgn}(\bar{c}) a] \frac{\text{sgn}(c)}{|c|} \end{aligned}$$

for any $a \in \mathbb{C}$ where \Im denotes the imaginary part. So we have

$$\lim_{\epsilon \rightarrow 0} \frac{1}{\epsilon} (\Gamma(u + \epsilon v) - \Gamma(u)) = \frac{1}{2} v + \frac{\rho - 1}{2(\rho + 1)} R_X v + \frac{\iota}{\rho + 1} \frac{b}{|x|} \odot \Omega \Im [\Omega^* R_X v]$$

which, in terms of $\eta = \Omega^* v$ and the notation (41), becomes Ω times J_A in (42). □

The following result says that for $\rho \geq 1$ all the non-solution fixed points are linearly unstable.

Theorem 5.2. *Let $\rho \geq 1$ and suppose that P_X is an orthogonal projection. Let u be a fixed point such that $x := R_X u$ has no vanishing components. Suppose*

$$(43) \quad \|J_A(\eta)\| \leq \|\eta\|, \quad \forall \eta \in \mathbb{C}^N.$$

Then

$$(44) \quad x = P_X x = b \odot \text{sgn}(x),$$

implying $u = x$ is a regular solution.

Proof. In view of Proposition 4.5, it suffices to show that $P_X^\perp x = 0$.

We prove the statement by contradiction. Suppose $P_X^\perp x \neq 0$.

By (32) and the Pythagoras theorem we have

$$(45) \quad \|P_X x\|_2^2 + \rho^2 \|P_X^\perp x\|^2 = \|b\|^2$$

and hence $\|b\| \geq \|x\|$ for $\rho \geq 1$. Applying Ω^* we rewrite (33) as

$$(46) \quad \tilde{P}_X |x| + \rho(|x| - \tilde{P}_X |x|) = \tilde{R}_X b$$

On the other hand, applying \tilde{P}_X on (46) we have

$$\tilde{P}_X |x| = \tilde{P}_X b$$

and hence by (46)

$$(47) \quad \tilde{P}_X |x| = \tilde{P}_X b = \frac{\rho|x|}{1+\rho} + \frac{b}{1+\rho}.$$

We now show that $\|J_A(\eta)\| > \|\eta\|$ if

$$(48) \quad \tilde{R}_X \eta = i\tilde{P}_X b = \frac{i\rho}{1+\rho}|x| + \frac{i}{1+\rho}b.$$

To this end, it is more convenient to write J_A in (42) in terms $\xi := \tilde{R}_X \eta$. With a slight abuse of notation we write

$$(49) \quad J_A(\xi) = \tilde{P}_X \xi - \frac{\xi}{\rho+1} + \frac{i}{\rho+1} \frac{b}{|x|} \odot \Im(\xi)$$

where we have used the properties in Proposition 4.1.

Since $\|\xi\| = \|\eta\|$, our goal is to show $\|J_A(\xi)\| > \|\xi\|$.

First we make an observation that will be useful later. We claim that

$$(50) \quad \rho\|x\|^2 = \|b\|^2 + (\rho-1)|x| \cdot b$$

where “ \cdot ” denote the (real) scalar product between two vectors. By (47),

$$\tilde{P}_X^\perp b = b - \tilde{P}_X b = \frac{\rho}{1+\rho}(|b| - |x|)$$

and hence by the Pythagoras theorem

$$\begin{aligned} \|b\|^2 &= \|\tilde{P}_X b\|^2 + \|\tilde{P}_X^\perp b\|^2 \\ &= \left\| \frac{\rho|x|}{1+\rho} + \frac{b}{1+\rho} \right\|^2 + \left\| \frac{\rho}{1+\rho}(|b| - |x|) \right\|^2 \\ &= \frac{2\rho^2}{(\rho+1)^2} \|x\|^2 + \frac{2\rho(1-\rho)}{(\rho+1)^2} |x| \cdot b + \frac{\rho^2+1}{(\rho+1)^2} \|b\|^2 \end{aligned}$$

which becomes (50) after rearrangement.

Next, note that by (48)

$$\tilde{P}_X \xi = \tilde{P}_X \eta = i\tilde{P}_X b = \xi,$$

which is purely imaginary, and hence

$$(51) \quad J_A(\xi) = \frac{\rho}{\rho+1}\xi + \frac{1}{\rho+1} \frac{b}{|x|} \odot \xi$$

by (49).

After some tedious but straightforward algebra with (48) and (51), we see that $\|J_A(\xi)\| > \|\xi\|$ is equivalent to the inequality

$$0 < (5\rho^2 - 2\rho - 1)\|b\|^2 + (2\rho^3 - 4\rho^2 - 2\rho)|x| \cdot b + 4\rho \frac{b}{|x|} \cdot b^2 + \left\| \frac{b^2}{|x|} \right\|^2 - \rho^2(2\rho + 1)\|x\|^2$$

which by (50) reduces to

$$(52) \quad 0 < (3\rho^2 - 3\rho - 1)\|b\|^2 - (3\rho^2 + \rho)|x| \cdot b + 4\rho \frac{b}{|x|} \cdot b^2 + \left\| \frac{b^2}{|x|} \right\|^2.$$

To proceed, we note that the assumption $\tilde{P}_X^\perp x \neq 0$ implies $|x| \neq b$, $\|x\| < \|b\|$ and moreover $|x|, b$ are not a multiple of each other. So by the Cauchy-Schwarz inequality we have

$$(53) \quad \left\| \frac{b^2}{|x|} \right\| > \frac{\|b\|^2}{\|x\|}, \quad \frac{b}{|x|} \cdot b^2 = \left\| \frac{b^{3/2}}{|x|^{1/2}} \right\|^2 > \frac{\|b\|^4}{\| |x|^{1/2} \odot b^{1/2} \|^2} = \frac{\|b\|^4}{|x| \cdot b}.$$

and hence the last two terms on the right hand side of (52) have the strict lower bound

$$(54) \quad \begin{aligned} 4\rho \frac{b}{|x|} \cdot b^2 + \left\| \frac{b^2}{|x|} \right\|^2 &> 4\rho \frac{\|b\|^4}{|x| \cdot b} + \frac{\|b\|^4}{\|x\|^2} \\ &> (1 + 4\rho)\|b\|^2 \end{aligned}$$

where we have used the fact $\|b\| \geq \|x\|$ due to $\rho \geq 1$.

In view of (54) the right hand side of (52) is strictly greater than

$$(3\rho^2 - 3\rho - 1)\|b\|^2 - (3\rho^2 + \rho)\|b\|^2 + (1 + 4\rho)\|b\|^2 = 0.$$

In other words, (52) holds indeed and the proof for $\|J_A(\xi)\| > \|\xi\|$ is complete.

This clearly contradicts the assumption (43). Therefore, $P_X^\perp x = 0$ and the desired result (44) follows from Propositions 4.4 and 4.5. □

The next result says that for any $\rho \geq 0$, all regular solutions are stable fixed points.

Theorem 5.3. *Let $\rho \geq 0$. Let u be a nonvanishing regular solution. Then*

$$(55) \quad \|J_A(\eta)\| \leq \|\eta\|$$

for all $\eta \in \mathbb{C}^N$ and the equality holds in the direction $\pm ib$ (and possibly elsewhere on the unit sphere).

Proof. By Proposition 4.4, $x := \tilde{R}_X u = u$ is a fixed point. By Proposition 4.5,

$$u = b \odot \text{sgn}(u) = Ag \quad \text{for some } g \in \mathbb{C}^{n^2}.$$

Rewriting $J_A(\eta)$ in (42) as

$$J_A(\eta) = \tilde{P}_X \eta - \frac{1}{\rho + 1} \tilde{R}_X \eta + \frac{i}{1 + \rho} \frac{b}{|x|} \odot \Im(\tilde{R}_X \eta)$$

and using $|x| = b$ we obtain

$$J_A(\eta) = \tilde{P}_X \eta - \frac{1}{1 + \rho} \Re(\tilde{R}_X \eta)$$

where \Re denotes the real part. We now show that $\|J_A(\eta)\| \leq \|\eta\|$ for all η .

To proceed, we shall write $\tilde{P}_X = HH^*$ where H is an isometry. This can be done for the matrix $C := \Omega^* A$ via the QR decomposition. In our setting, the measurement matrix of each diffraction pattern has orthogonal columns and so does the total measurement matrix. Hence the R factor of C is a diagonal matrix with the norms of the columns of C on the diagonal (see Appendix A). For ease of notation, we may assume that $\Omega^* A = H$.

Note that

$$(56) \quad \begin{bmatrix} \Re[H] & -\Im[H] \\ \Im[H] & \Re[H] \end{bmatrix}$$

is real isometric because H is complex isometric. Define

$$(57) \quad \mathcal{H} := \begin{bmatrix} \Re[H^*] \\ \Im[H^*] \end{bmatrix} \in \mathbb{R}^{2n^2 \times N}.$$

By Proposition D.4 and Corollary D.5 in Appendix D, HH^* can be block-diagonalized into one $(N - 2n^2) \times (N - 2n^2)$ zero block and $2n^2$ 2×2 blocks

$$(58) \quad \begin{bmatrix} \lambda_k^2 & \lambda_k \lambda_{2n^2+1-k} \\ \lambda_k \lambda_{2n^2+1-k} & \lambda_{2n^2+1-k}^2 \end{bmatrix}, \quad k = 1, 2, \dots, 2n^2$$

in the orthonormal basis $\{\eta_k, \nu_{2n^2+1-k} : k = 1, 2, \dots, 2n^2\}$ where $\eta_k \in \mathbb{R}^N$ are the right singular vectors, corresponding to the singular values λ_k , of \mathcal{H} .

Moreover, the complete set of singular values satisfy

$$(59) \quad 1 = \lambda_1 \geq \lambda_2 \geq \dots \geq \lambda_{2n^2} = \lambda_{2n^2+1} = \dots = \lambda_N = 0$$

$$(60) \quad \lambda_k^2 + \lambda_{2n^2+1-k}^2 = 1.$$

In view of the block-diagonal nature of HH^* , we shall analyze $J_A(\eta)$ in the 2-dim spaces spanned by the orthonormal basis $\{\eta_k, \nu_{2n^2+1-k}\}$ one k at a time.

For any fixed k and

$$\eta = z_1 \eta_k + i z_2 \nu_{2n^2+1-k}, \quad z_1, z_2 \in \mathbb{C},$$

we obtain

$$(61) \quad J_A(\eta) = (\lambda_k^2 z_1 + \lambda_k \lambda_{2n^2+1-k} z_2) \eta_k + (\lambda_k \lambda_{2n^2+1-k} z_1 + \lambda_{2n^2+1-k}^2 z_2) v \eta_{2n^2+1-k} \\ + \frac{1}{1+\rho} [(1 - 2\lambda_k^2) \Re(z_1) - 2\lambda_k \lambda_{2n^2+1-k} \Re(z_2)] \eta_k \\ + \frac{1}{1+\rho} [2\lambda_k \lambda_{2n^2+1-k} \Im(z_1) - (1 - 2\lambda_{2n^2+1-k}^2) \Im(z_2)] \eta_{2n^2+1-k}.$$

Next we treat (61) as a linear function of $\Re(z_1), \Re(z_2), \Im(z_1), \Im(z_2)$ with real coefficients in the basis $\{\eta_k, v\eta_{2n^2+1-k}, v\eta_k, \eta_{2n^2+1-k}\}$ and represent J_A by a 4×4 matrix which is block-diagonalized into two 2×2 blocks:

$$(62) \quad \begin{bmatrix} \frac{1}{1+\rho} + \frac{\rho-1}{\rho+1} \lambda_k^2 & \frac{\rho-1}{\rho+1} \lambda_k \lambda_{2n^2+1-k} \\ \lambda_k \lambda_{2n^2+1-k} & \lambda_{2n^2+1-k}^2 \end{bmatrix}, \quad \begin{bmatrix} \lambda_k^2 & \lambda_k \lambda_{2n^2+1-k} \\ -\frac{\rho-1}{\rho+1} \lambda_k \lambda_{2n^2+1-k} & -\frac{1}{\rho+1} - \frac{\rho-1}{\rho+1} \lambda_{2n^2+1-k}^2 \end{bmatrix}.$$

with the former of (62) acting on $\Re(z_1), \Re(z_2)$ and the latter acting on $\Im(z_1), \Im(z_2)$. In view of their similar structure, it suffices to focus on the former.

The eigenvalues of the first matrix in (62) are

$$(63) \quad \frac{1}{2(\rho+1)} \left[\rho + 2(1 - \lambda_k^2) \pm \sqrt{\rho^2 - 4\lambda_k^2 + 4\lambda_k^4} \right]$$

which, with the + sign, equals 1 at $k = 2n^2$ (recall $\lambda_{2n^2} = 0$). Next we show that 1 is the largest eigenvalue among all k and $\rho \in [0, \infty)$.

Note that (63) is real-valued for any $\lambda_k \in [0, 1]$ iff $\rho \geq 1$. Hence, for $\rho \geq 1$, the maximum eigenvalue is 1 and occurs at $k = 2n^2$.

For $\rho < 1$ and $\rho^2 - 4\lambda_k^2 + 4\lambda_k^4 \geq 0$, the maximum value of (63) can be bounded as

$$(64) \quad \frac{1}{2(\rho+1)} \left[\rho + 2(1 - \lambda_k^2) + \sqrt{\rho^2 - 4\lambda_k^2 + 4\lambda_k^4} \right] \\ = \frac{1}{2(\rho+1)} \left[\rho + 2(1 - \lambda_k^2) + \sqrt{\rho^2 - 4\lambda_k^2(1 - \lambda_k^2)} \right] \\ \leq \frac{1}{2(\rho+1)} [\rho + 2(1 - \lambda_k^2) + \rho] \\ = 1 - \frac{\lambda_k^2}{\rho+1} \leq 1$$

since $4\lambda_k^2(1 - \lambda_k^2) \geq 0$. Hence the expression (63) achieves the maximum value 1 at $k = 2n^2$.

For $\rho < 1$ and $\rho^2 - 4\lambda_k^2 + 4\lambda_k^4 \leq 0$, the modulus of (63) equals

$$(65) \quad \sqrt{\frac{1 - \lambda_k^2}{1 + \rho}} \leq 1.$$

By Proposition D.1, $\eta_1 = b$, $\tilde{P}_X(ib) = ib$, $\tilde{R}_X(ib) = ib$ and hence $J_A(ib) = ib$. However, $\arg \max_{\|\eta\|=1} |J_A(\eta)|$ may contain points other than $\pm ib/\|b\|$ since we do not know if $\lambda_2 < 1$ without additional conditions (see Section 6). The proof is complete.

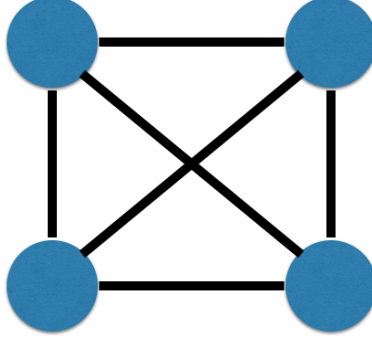


FIGURE 2. A complete undirected graph corresponding to the regular raster scan with 4 blocks overlapping with one another.

□

6. SPECTRAL GAP

In this section, we derive the optimal parameter ρ_* that produces the largest spectral gap ($\lambda_2 - \lambda_1$) at a regular solution (Corollary 6.2) and show that Gaussian-DRS with $\rho = 1$ has the same convergence rate at a regular solution as AP which is smaller than CDR (Corollary 6.4).

To derive a positive spectral gap $\lambda_2 < \lambda_1 = 1$, we need some details of the ptychographic set-up (Appendix A).

Let \mathcal{T} be the set of all shifts, including $(0, 0)$, involved in the ptychographic measurement. Denote by $\mu^{\mathbf{t}}$ the \mathbf{t} -shifted probe for all $\mathbf{t} \in \mathcal{T}$ and $\mathcal{M}^{\mathbf{t}}$ the domain of $\mu^{\mathbf{t}}$. Let $f^{\mathbf{t}}$ the object restricted to $\mathcal{M}^{\mathbf{t}}$. For convenience, we assume the periodic boundary condition on the whole object domain $\mathcal{M} = \cup_{\mathbf{t} \in \mathcal{T}} \mathcal{M}^{\mathbf{t}}$ when $\mu^{\mathbf{t}}$ crosses over the boundary of \mathcal{M} .

Two blocks $\mathcal{M}^{\mathbf{t}}$ and $\mathcal{M}^{\mathbf{t}'}$ are said to be connected if the minimum overlap condition

$$\#\{\mathcal{M}^{\mathbf{t}} \cap \mathcal{M}^{\mathbf{t}'} \cap \text{supp}(f)\} \geq 2$$

is satisfied. Let \mathcal{G} be the undirected graph with the nodes corresponding to $\{\mathcal{M}^{\mathbf{t}} : \mathbf{t} \in \mathcal{T}\}$ and the edges between any pair of connected nodes (see Figure 2).

Now we recall the following spectral gap theorem [9] (Proposition 3.5 and the subsequent remark).

Proposition 6.1. [9] *In addition to the above assumptions, suppose $\text{supp}(f)$ is not a subset of a line. Let u (and hence $x := R_X u$) be a regular solution. Let λ_2 be the second largest singular value of \mathcal{H} defined in (57). If the graph \mathcal{G} is connected, then $\lambda_2 < 1$.*

Using Proposition 6.1, we can sharpen the result of Theorem 5.3 as follows.

Corollary 6.2. *Under the assumptions of Proposition 6.1, the second largest singular value of J_A is strictly less than 1 and achieves the minimum value*

$$(66) \quad \frac{\lambda_2}{\sqrt{1 + 2\lambda_2\sqrt{1 - \lambda_2^2}}} \quad \text{at} \quad \rho_* = 2\lambda_2\sqrt{1 - \lambda_2^2} \leq 1.$$

Moreover, the second largest singular value of J_A is an increasing function of ρ in the range $[\rho_*, \infty)$ and a decreasing function in the range of $[0, \rho_*]$.

Remark 6.3. *By arithmetic-geometric-mean inequality,*

$$\rho_* \leq 2 \times \frac{1}{2}(\lambda_2^2 + 1 - \lambda_2^2) = 1$$

where the equality holds only when $\lambda_2^2 = 1/2$.

As λ_2^2 tends to 1, ρ_* tends to 0 and as λ_2^2 tends to $\frac{1}{2}$, ρ_* tends to 1.

Unfortunately, since λ_2 depends on the generalized solution u , it is impossible to calculate λ_2 without knowing u .

Proof. Our discussion splits into several cases. By $\lambda_2^2 = 1 - \lambda_{2n^2-1}^2$, we have $\lambda_2^2(1 - \lambda_2^2) = \lambda_{2n^2-1}^2(1 - \lambda_{2n^2-1}^2)$ and $\lambda_2^2 \geq 1/2$.

For $\rho > 1$, the larger eigenvalue in (63) achieves the second largest value

$$(67) \quad \frac{1}{2(1 + \rho)} \left[\rho + 2\lambda_2^2 + \sqrt{\rho^2 - 4\lambda_2^2(1 - \lambda_2^2)} \right]$$

at $k = 2n^2 - 1$ after some algebra. The expression (67) is strictly less than

$$\frac{1}{2(1 + \rho)} [2\rho + 2\lambda_2^2] = \frac{\rho + \lambda_2^2}{\rho + 1} < 1$$

with the spectral gap $\lambda_2 < 1$.

For $\rho = 1$, (63) becomes

$$(68) \quad \frac{1}{4} [1 + 2(1 - \lambda_k^2) \pm |1 - 2\lambda_k^2|]$$

which achieves the second largest value

$$(69) \quad 1 - \lambda_{2n^2-1}^2 = \lambda_2^2 < 1$$

at $k = 2n^2 - 1$ by (60).

The case of $\rho < 1$ requires more analysis since the eigenvalue (63) may be real or complex. Analyzing as in (64) and (65) we conclude that the second largest value is

$$(70) \quad \frac{1}{2(\rho + 1)} \left[\rho + 2\lambda_2^2 + \sqrt{\rho^2 - 4\lambda_2^2(1 - \lambda_2^2)} \right] \quad \text{if} \quad \rho \geq \rho_* = 2\lambda_2\sqrt{1 - \lambda_2^2}$$

and

$$(71) \quad \frac{\lambda_2}{\sqrt{1 + \rho}} \quad \text{if} \quad \rho \leq \rho_*$$

While the expression in (71) is a decreasing function of ρ and less than λ_2 , (70) is an increasing function of ρ and less than (69) for $\rho = 1$.

Also, for $\rho > 1$, the expression (67), as a function of ρ , has the derivative

$$\frac{1}{2(\rho+1)^2} \left[1 - 2\lambda_2^2 + \frac{\rho + 4\lambda_2^2(1 - \lambda_2^2)}{\sqrt{\rho^2 - 4\lambda_2^2(1 - \lambda_2^2)}} \right] > \frac{1}{2(\rho+1)^2} [2 - 2\lambda_2^2] > 0$$

and hence achieves the minimum at $\rho = 1$. In other words, DRS with $\rho = 1$ converges faster than DRS with $\rho > 1$.

From the preceding analysis, the second largest singular value achieves the minimum at the crossover value ρ_* of the two expression in (70). Substituting ρ_* in (70) we arrive at (66).

Although it is not immediately obvious, it can be verified by calculus that (66) is less than λ_2^2 (for $\rho = 1$).

□

For comparison with CDR, we note that for $\rho = 0$ (71) is exactly λ_2 and greater than λ_2^2 in (69) for $\rho = 1$, which coincides with the convergence rate of Alternating Projections (AP).

Corollary 6.4. *For $\rho = 1$, the local convergence rate is given by λ_2^2 which is smaller than the convergence rate λ_2 for $\rho = 0$.*

This implies that locally Gaussian-DRS with $\rho = 1$ converges faster than CDR and as fast as AP.

With a positive spectral gap, this largest eigenvalue 1 in Theorem 5.3 corresponds to the global phase factor and Corollary 6.2 can be used to prove local, linear convergence for Gaussian DRS with $\rho \geq 0$. The proof is analogous to that given in [8, 9] for CDR ($\rho = 0$) and omitted here.

7. OPTIMAL STEP SIZE

The preceding fixed point analysis provides a guideline for selection of the step size.

First, Theorem 4.6 and Corollary 4.9 suggest that the Gaussian-DRS with $\rho \in [1, \infty)$ may be more stable than with $\rho \in [0, 1)$. This is further confirmed by Theorem 5.2 which says no fixed points other than the regular solution(s) are locally stable for the range $\rho \geq 1$ (It is unclear if this property holds for $\rho < 1$).

Second, Gaussian-DRS with $\rho = 1$ produces the optimal convergence rate for the range $\rho \geq 1$ (Corollary (6.2) and Remark 6.3) which is smaller than that of CDR (Corollary 6.4) but the same as AP [10].

Finally, for $\rho = 1$, the fixed point equation (26) reduces to

$$(72) \quad u = b \odot \operatorname{sgn}(R_X u)$$

and hence any fixed point u satisfies

$$(73) \quad |u| = b$$

$$(74) \quad \text{sgn}(u) = \text{sgn}(R_X u) \quad \text{whenever } b > 0.$$

In contrast, the fixed points (12) of CDR have the true phase $\text{sgn}(Af)$ while compromise on the magnitude. The property (73) means that $u[j] \neq 0$ whenever $b[j] > 0$ for all j . An advantage with randomly phased probes is that $b > 0$ almost certainly [8]. The absence of degenerate fixed points for $\rho = 1$ alleviates some of the numerical problems associated with CDR (cf. remarks at the end of Section 2).

In summary, a main implication of the fixed point analysis is the choice $\rho = 1$, giving rise to the Gaussian DRS-map

$$(75) \quad \Gamma(u) = \frac{1}{2}u + \frac{1}{2}P_Y x, \quad x := R_X u$$

(since \mathcal{R}_Y in (19) is exactly P_Y with $\rho = 1$). The contrast between (75) and the CDR map (2) is noteworthy. The simplicity of the form (75) suggests the name *Averaged Projection Reflection* (APR) algorithm. The corresponding Poisson DRS map Π , however, is not as simple:

$$(76) \quad \Pi(u) = \frac{1}{2}u + \frac{1}{6} \left[\sqrt{|x|^2 + 24b^2} - 2|x| \right] \odot \text{sgn}(x).$$

8. APPLICATION: BLIND PTYCHOGRAPHY

In this section we apply the optimal DRS schemes to the more challenging problem of blind ptychography. In blind ptychography, we do not assume the full knowledge of the probe which is to be recovered simultaneously with the unknown object.

Let ν^0 and $g = \vee_{\mathbf{t}} g^{\mathbf{t}}$ be any pair of the probe and the object estimates producing the same ptychography data as μ^0 and f , i.e. the diffraction pattern of $\nu^{\mathbf{t}} \odot g^{\mathbf{t}}$ is identical to that of $\mu^{\mathbf{t}} \odot f^{\mathbf{t}}$ where $\nu^{\mathbf{t}}$ is the \mathbf{t} -shift of ν^0 and $g^{\mathbf{t}}$ is the restriction of g to $\mathcal{M}^{\mathbf{t}}$. We refer to the pair (ν^0, g) as a blind-ptychographic solution (in the object domain) and (μ^0, f) as the true solution.

We can write the total measurement data as $b = |\mathcal{F}(\mu^0, f)|$ where \mathcal{F} is the concocted oversampled Fourier transform acting on $\{\mu^{\mathbf{t}} \odot f^{\mathbf{t}} : \mathbf{t} \in \mathcal{T}\}$ (see Appendix A), i.e. a bi-linear transformation in the direct product of the probe space and the object space. By definition, a blind-ptychographic solution (ν^0, g) satisfies $|\mathcal{F}(\nu^0, g)| = b$.

There are two ambiguities inherent to any blind ptychography.

The first is the affine phase ambiguity. Consider the probe and object estimates

$$(77) \quad \nu^0(\mathbf{n}) = \mu^0(\mathbf{n}) \exp(-ia - i\mathbf{w} \cdot \mathbf{n}), \quad \mathbf{n} \in \mathcal{M}^0$$

$$(78) \quad g(\mathbf{n}) = f(\mathbf{n}) \exp(ib + i\mathbf{w} \cdot \mathbf{n}), \quad \mathbf{n} \in \mathbb{Z}_n^2$$

for any $a, b \in \mathbb{R}$ and $\mathbf{w} \in \mathbb{R}^2$. For any \mathbf{t} , we have the following calculation

$$\begin{aligned}\nu^{\mathbf{t}}(\mathbf{n}) &= \nu^0(\mathbf{n} - \mathbf{t}) \\ &= \mu^0(\mathbf{n} - \mathbf{t}) \exp(-i\mathbf{w} \cdot (\mathbf{n} - \mathbf{t})) \exp(-ia) \\ &= \mu^{\mathbf{t}}(\mathbf{n}) \exp(-i\mathbf{w} \cdot (\mathbf{n} - \mathbf{t})) \exp(-ia)\end{aligned}$$

and hence for all $\mathbf{n} \in \mathcal{M}^{\mathbf{t}}, \mathbf{t} \in \mathcal{T}$

$$(79) \quad \nu^{\mathbf{t}}(\mathbf{n})g^{\mathbf{t}}(\mathbf{n}) = \mu^{\mathbf{t}}(\mathbf{n})f^{\mathbf{t}}(\mathbf{n}) \exp(i(b - a)) \exp(i\mathbf{w} \cdot \mathbf{t}).$$

Clearly, (79) implies that g and ν^0 produce the same ptychographic data as f and μ^0 since for each \mathbf{t} , $\nu^{\mathbf{t}} \odot g^{\mathbf{t}}$ is a constant phase factor times $\mu^{\mathbf{t}} \odot f^{\mathbf{t}}$ where \odot is the entry-wise (Hadamard) product. It is also clear that the above statement holds true regardless of the set \mathcal{T} of shifts and the type of probe.

In addition to the affine phase ambiguity (77)-(78), a scaling factor ($g = cf, \nu^0 = c^{-1}\mu^0, c > 0$) is inherent to any blind ptychography. Note that when the probe is exactly known (i.e. $\nu^0 = \mu^0$), neither ambiguity can occur.

Besides the inherent ambiguities, blind ptychography imposes extra demands on the scanning scheme. For example, there are many other ambiguities inherent to the regular raster scan: $\mathcal{T} = \{\mathbf{t}_{kl} = \tau(k, l) : k, l \in \mathbb{Z}\}$ unless the step size $\tau = 1$. Blind ptychography with a raster scan produces τ -periodic ambiguities called the raster scan pathology as well as non-periodic ambiguities associated with block phase drift. The reader is referred to [15] for a complete analysis of ambiguities associated with the raster scan.

A conceptually simple (though not necessarily the most practical) way to remove these ambiguities is introducing small irregular perturbations to the raster scan with $\tau > m/2$, i.e. the overlap ratio greater than 50% (see (86) and (87)). For a thorough analysis of the conditions for blind ptychography, we refer the reader to [15, 16].

The basic strategy for blind ptychographic reconstruction is to alternately update the object and probe estimates starting from an initial guess as outlined in Algorithm 1 [17, 42, 43].

Algorithm 1: Alternating minimization (AM)

- 1: Input: initial probe guess μ_1 and object guess f_1 .
 - 2: Update the object estimate $f_{k+1} = \arg \min L(A_k g)$ s.t. $g \in \mathbb{C}^{n \times n}$.
 - 3: Update the probe estimate $\mu_{k+1} = \arg \min L(B_k \nu)$ s.t. $\nu \in \mathbb{C}^{m \times m}$.
 - 4: Terminate if $\| |B_k \mu_{k+1}| - b \|$ stagnates or is less than tolerance; otherwise, go back to step 2 with $k \rightarrow k + 1$.
-

We solve the inner loops (step 2 and 3 in Algorithm 1) and update the object and probe estimates by the DRS methods where $A_k h := \mathcal{F}(\mu_k, h), \forall h \in \mathbb{C}^{n^2}$, defines a matrix A_k for the k -th probe estimate μ_k and $B_k \eta := \mathcal{F}(\eta, f_{k+1}), \forall \eta \in \mathbb{C}^{m^2}$, for the $(k + 1)$ -st image estimate f_{k+1} . Both A_k and B_k can be put in the form of ΨD where Ψ is an isometry (concocted oversampled Fourier transforms) and D is a diagonal matrix (including the probe and object estimates, respectively, as well as column normalization).

For ease of reference, we denote Algorithm 1 with Gaussian-DRS and Poisson-DRS by Gaussian DRSAM and Poisson DRSAM, respectively.

8.1. Initialization. For non-convex iterative optimization, a good initial guess or some regularization is usually crucial for convergence [4, 44]. The initialization step is often glossed over in the development of numerical schemes. This is even more so for blind ptychography which is doubly non-convex because, in addition to the phase retrieval step, extracting the probe and the object from their product is also non-convex.

Our initialization method relies on a prior on the probe inspired by the uniqueness theory in [16].

We say that a probe estimate ν^0 satisfies PPC (standing for the probe phase constraint) if

$$(80) \quad \angle(\nu^0(\mathbf{n}), \mu^0(\mathbf{n})) < \delta\pi, \quad \forall \mathbf{n}$$

where $\delta \in (0, 1/2]$ is the uncertainty parameter.

PPC defines an alternative measure to the standard norm-based metric. Our default case is $\delta = 0.5$ with which PPC $\Re(\bar{\nu}^0 \odot \mu^0) > 0$ (where the bar denotes the complex conjugate) has the intuitive meaning that at every pixel ν^0 and μ^0 point to the same half plane in \mathbb{C} .

Under PPC, however, the initial probe may be significantly far away from the true probe in norm. Even if $|\mu_1(\mathbf{n})| = |\mu^0(\mathbf{n})| = \text{const.}$, the probe guess with uniformly distributed ϕ in $(-\pi/2, \pi/2]$ has the relative error close to

$$\sqrt{\frac{1}{\pi} \int_{-\pi/2}^{\pi/2} |e^{i\phi} - 1|^2 d\phi} = \sqrt{2\left(1 - \frac{2}{\pi}\right)} \approx 0.8525$$

with high probability. We use (80) for selecting and quantifying initialization, instead of the usual 2-norm. The non-blind ptychography gives rise to infinitesimally small δ . In practice, (80) needs only to hold for sufficiently large number of pixels \mathbf{n} .

For greater generality, we also want to allow for the unavoidable affine phase ambiguity and the scaling ambiguity. To this end, we consider the following probe initialization denoted by PPC(\mathbf{k}, δ)

$$(81) \quad \mu_1(\mathbf{n}) = \mu^0(\mathbf{n}) \exp \left[i2\pi \frac{\mathbf{k} \cdot \mathbf{n}}{n} \right] \exp [i\phi(\mathbf{n})], \quad \mathbf{n} \in \mathcal{M}^0$$

where $\phi(\mathbf{n})$ are independently and uniformly distributed on $(-\delta\pi, \delta\pi)$. In our numerical experiments, PPC($\mathbf{k}, 0.5$) results in fast geometric convergence for any \mathbf{k} .

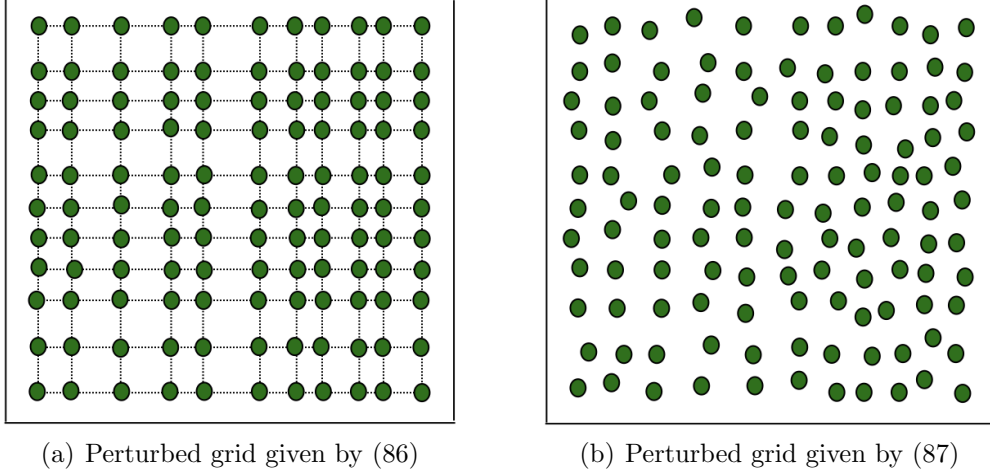


FIGURE 3. Two perturbed raster scans

9. NUMERICAL EXPERIMENTS

In this section, we test the performance of the Gaussian and Poisson DRSAM with $\rho = 1$. The inner loops of Gaussian DRSAM become

$$\begin{aligned} u_k^{l+1} &= \frac{1}{2}u_k^l + \frac{1}{2}b \odot \text{sgn}(R_k u_k^l) \\ v_k^{l+1} &= \frac{1}{2}v_k^l + \frac{1}{2}b \odot \text{sgn}(S_k v_k^l). \end{aligned}$$

and the inner loops of the Poisson DRSAM become

$$(82) \quad u_k^{l+1} = \frac{1}{2}u_k^l - \frac{1}{3}R_k u_k^l + \frac{1}{6}\text{sgn}(R_k u_k^l) \odot \sqrt{|R_k u_k^l|^2 + 24b^2}$$

$$(83) \quad v_k^{l+1} = \frac{1}{2}v_k^l - \frac{1}{3}S_k v_k^l + \frac{1}{6}\text{sgn}(S_k v_k^l) \odot \sqrt{|S_k v_k^l|^2 + 24b^2}.$$

Here $R_k = 2P_k - I$ is the reflector corresponding to the projector $P_k := A_k A_k^\dagger$ and S_k is the reflector corresponding to the projector $Q_k := B_k B_k^\dagger$. We set $u_k^1 = u_{k-1}^\infty$ where u_{k-1}^∞ is the terminal value at epoch $k-1$ and $v_k^1 = v_{k-1}^\infty$ where v_{k-1}^∞ is the terminal value at epoch $k-1$.

9.1. Error metrics. We use relative error (RE) and relative residual (RR) as the merit metrics for the recovered image f_k and probe μ_k at the k^{th} epoch:

$$(84) \quad \text{RE}(k) = \min_{\alpha \in \mathbb{C}, \mathbf{k} \in \mathbb{R}^2} \frac{\|f(\mathbf{k}) - \alpha e^{-i2\pi \mathbf{k} \cdot \mathbf{r}/n} f_k(\mathbf{k})\|}{\|f\|}$$

$$(85) \quad \text{RR}(k) = \frac{\|b - |A_k f_k|\|}{\|b\|}.$$

Note that in (84) both the affine phase and the scaling factors are discounted.

9.2. Sampling schemes. The uniqueness theorem [15] holds for the following irregular raster scans

$$(86) \quad \text{Rank-one perturbation} \quad \mathbf{t}_{kl} = \tau(k, l) + (\delta_k^1, \delta_l^2), \quad k, l \in \mathbb{Z}$$

where δ_k^1 and δ_l^2 are small random variables relative to τ . The other is

$$(87) \quad \text{Full-rank perturbation} \quad \mathbf{t}_{kl} = \tau(k, l) + (\delta_{kl}^1, \delta_{kl}^2), \quad k, l \in \mathbb{Z}$$

where δ_{kl}^1 and δ_{kl}^2 are small random variables relative to τ . Here the stepsize $\tau < m/2$ corresponding to the overlap ratio smaller than 50%.

We let δ_k^1 and δ_l^2 in the rank-one scheme (86) and δ_{kl}^1 and δ_{kl}^2 in the full-rank scheme (87) to be i.i.d. uniform random variables over $\llbracket -4, 4 \rrbracket$. In other words, the adjacent probes overlap by an average of $\tau/m = 50\%$.

9.3. Probe function. We use a randomly phased probe with the unknown transmission function $\mu^0(\mathbf{n}) = |\mu^0(\mathbf{n})|e^{i\theta(\mathbf{n})}$ where $\theta(\mathbf{n})$ are random variables and $|\mu^0(\mathbf{n})| \neq 0, \forall \mathbf{n} \in \mathcal{M}^0$. Randomly phased probes have been adopted in ptychographic experiments [32, 34, 38, 41].

We do not explore the issue of varying the probe size in the present work, which has been done for CDR in [9]. We fix the probe size to 60×60 . In addition to the i.i.d. probe, we consider also correlated probe produced by convolving the i.i.d. probe with characteristic function of the set $\{(k_1, k_2) \in \mathbb{Z}^2 : \max\{|k_1|, |k_2|\} \leq c \cdot m; c \in (0, 1]\}$ where the constant c is a measure of the correlation length in the unit of $m = 60$ (Fig. 4).

9.4. Test objects. Our first test image is 256-by-256 Cameraman+ i Barbara (CiB). The resulting test object has the phase range $\pi/2$. The second test object is randomly-phased phantom (RPP) defined by $f_* = P \odot e^{i\phi}$ where P is the standard phantom (Fig. 6(a)) and $\{\phi(\mathbf{n})\}$ are i.i.d. uniform random variables over $[0, 2\pi]$. RPP has the maximal phase range because of its noise-like phase profile. In addition to the huge phase range, RPP has loosely supported parts with respect to the measurement schemes (see below) due to its thick dark margins around the oval.

9.5. Different combinations. First we compare performance of DRSAM with different combinations of objective functions, scanning schemes and random probes in the case of noiseless measurements with the periodic boundary condition. We use the stopping criteria for the inner loops:

$$\frac{\| |A_k A_k^\dagger u_k^l| - b \| - \| |A_k A_k^\dagger u_k^{l+1}| - b \|}{\| |A_k A_k^\dagger u_k^l| - b \|} \leq 10^{-4}$$

with the maximum number of iterations capped at 60.

Figure 7 shows geometric decay of RE (84) at various rates r_o for the test object CiB. In particular, Fig. 7(a) shows that the full-rank scheme outperforms the rank-one scheme and that Poisson-DRS outperforms (slightly) Gaussian-DRS while Figure 7(b) shows that the i.i.d. probe yields the smallest rate of convergence ($r_o = 0.7562$) closely followed by the rate ($r_o = 0.7583$) for $c = 0.4$.

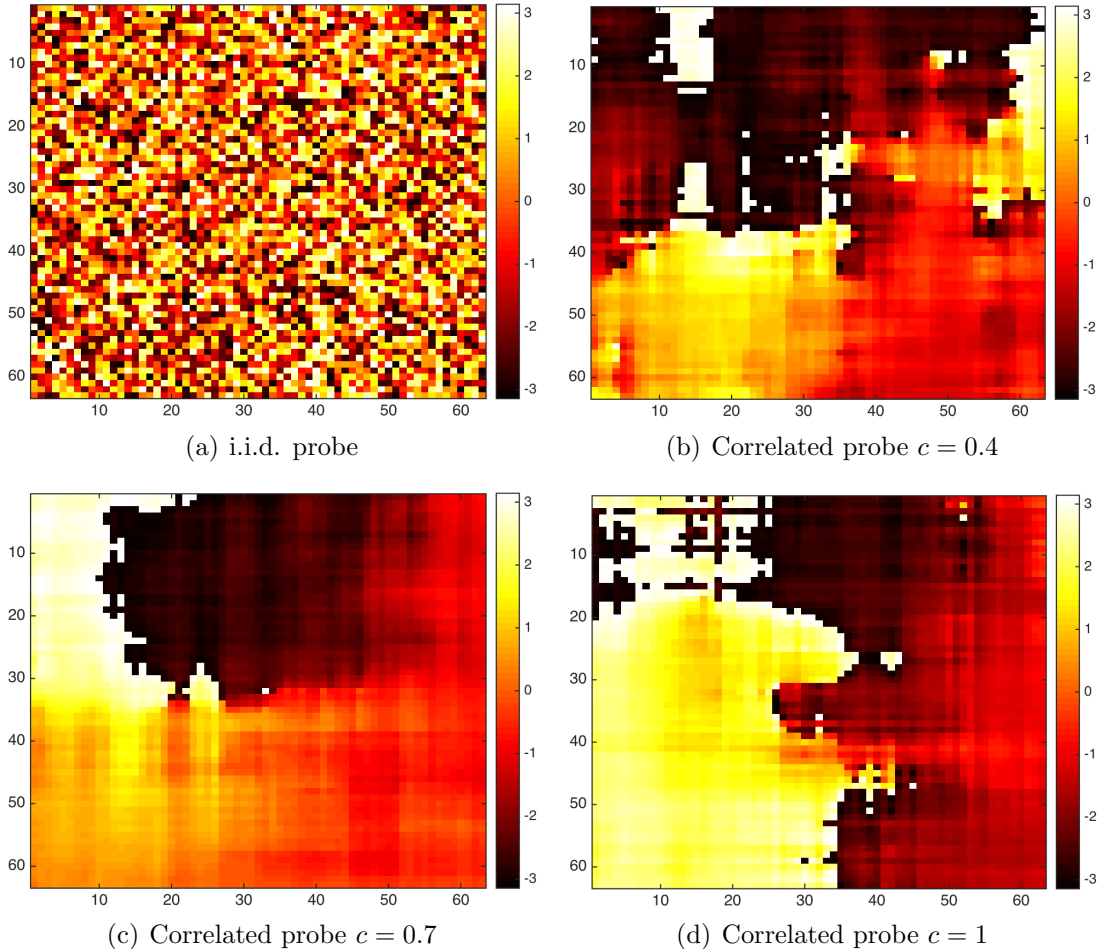


FIGURE 4. The phase profile of (a) the i.i.d. probe and (b)(c)(d) the correlated probes of various correlation lengths.

9.6. **Poisson noise.** For noisy measurement, the level of noise is measured in terms of the noise-to-signal ratio (NSR).

$$\text{NSR} = \frac{\|b - |Af|\|}{\|Af\|}$$

where A is the true measurement matrix and f the true object.

Figure 8(b) shows RE (84) for CiB versus NSR for Poisson-DRS and Gaussian-DRS with the periodic boundary condition, i.i.d. probe and the full-rank scheme. The maximum number of epoch in DRSAM is limited to 100. The RR stabilizes usually after 30 epochs. The (blue) reference straight line has slope 1. We see that the Gaussian-DRS outperforms the Poisson-DRS, especially when the Poisson RE becomes unstable for $\text{NSR} \geq 35\%$. As noted in [10, 31, 50] fast convergence (with the Poisson log-likelihood function) may introduce noisy artifacts and reduce reconstruction quality.

For the rest of the experiments, we use noiseless data, Poisson-DRS and the full-rank scheme.



(a)

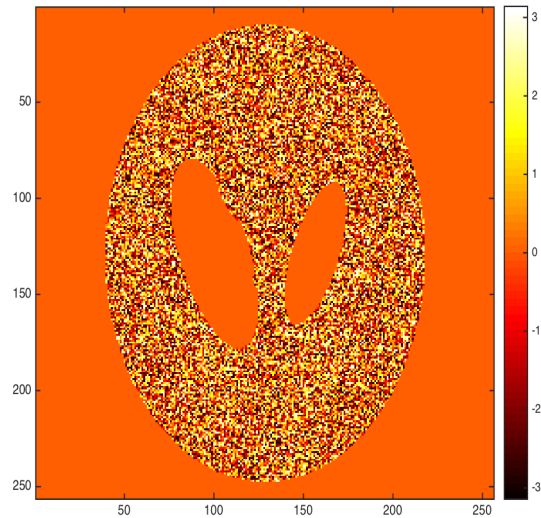


(b)

FIGURE 5. (a) The real part and (b) the imaginary part of the test image CiB.



(a) RPP magnitudes



(b) RPP phases

FIGURE 6. (a) Magnitudes and (b) phases of RPP.

9.7. Boundary conditions. The periodic boundary condition conveniently treats all diffraction patterns and object pixels in the same way by assuming that \mathbb{Z}_n^2 is a (discrete) torus. The periodic boundary condition generally forces the slope \mathbf{r} in the affine phase ambiguity to be integers. In contrast, the non-periodic bright-field boundary conditions assumes nonzero values in $\mathcal{M} \setminus \mathbb{Z}_n^2$.

To show that the affine phase ambiguity is absent under the bright-field boundary condition, we test DRSAM with the initialization $\text{PPC}(-0.5, 0.5, \frac{1}{2})$ and use a more stringent error

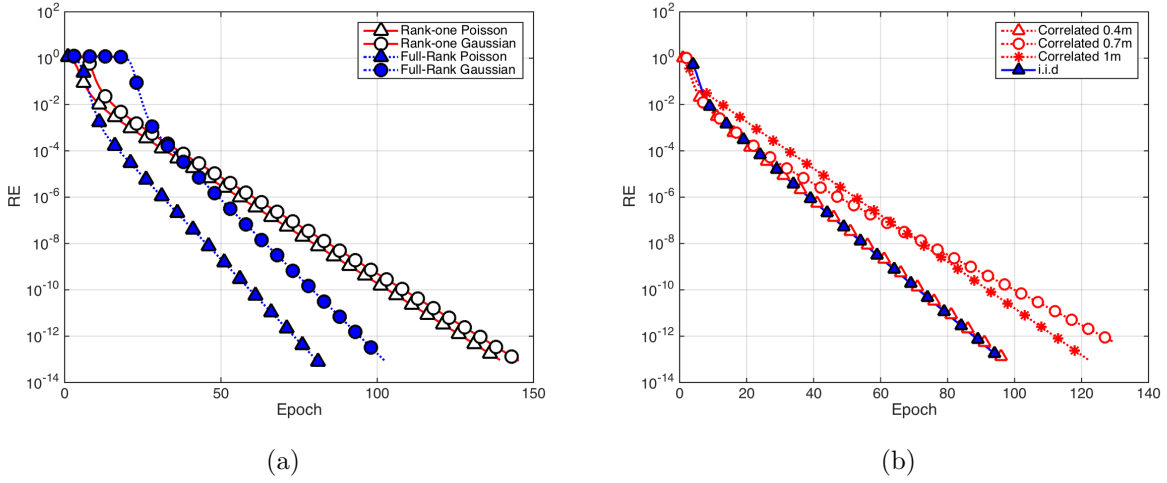


FIGURE 7. Geometric convergence to CiB at various rates for (a) Four combinations of objective functions and scanning schemes with i.i.d. probe (rank-one Poisson, $r_o = 0.8236$; rank-one Gaussian, $r_o = 0.8258$; full-rank Poisson, $r_o = 0.7205$; full-rank Gaussian, $r_o = 0.7373$) and (b) Poisson-DRS with four probes of different correlation lengths ($r_o = 0.7583$ for $c = 0.4$; $r_o = 0.8394$ for $c = 0.7$; $r_o = 0.7932$ for $c = 1$; $r_o = 0.7562$ for iid probe)

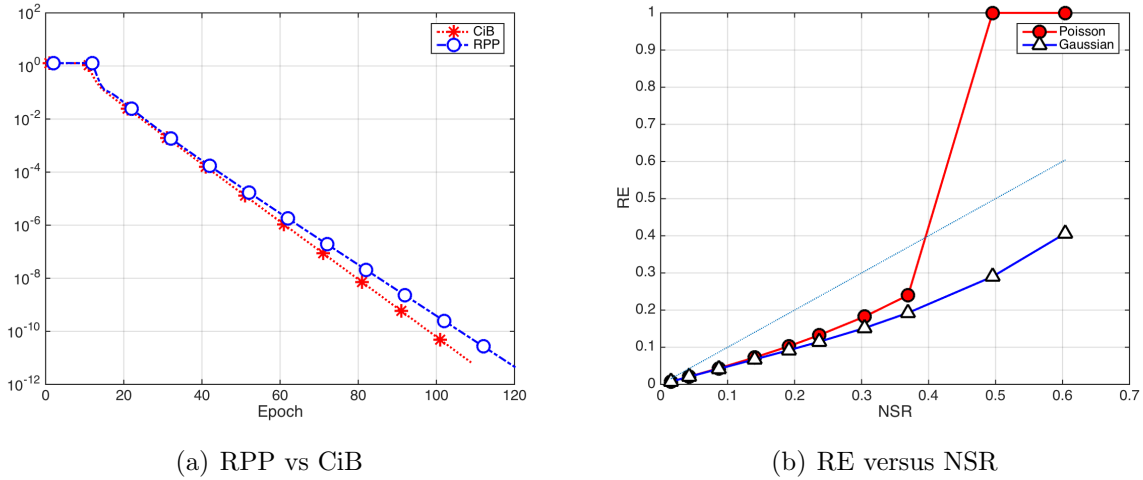


FIGURE 8. PPC(-1,1,0.5) RPP and CiB: Blue circle: Rate = 0.8015, $\mathbf{k}_{im} = (-1, 1.0517)$; Red star: Rate=0.7787, $\mathbf{k}_{im} = (-1, 1)$

metric

$$(88) \quad \text{RE2}(k) = \min_{\alpha \in \mathbb{C}} \frac{\|f(\mathbf{k}) - \alpha f_k(\mathbf{k})\|}{\|f\|}.$$

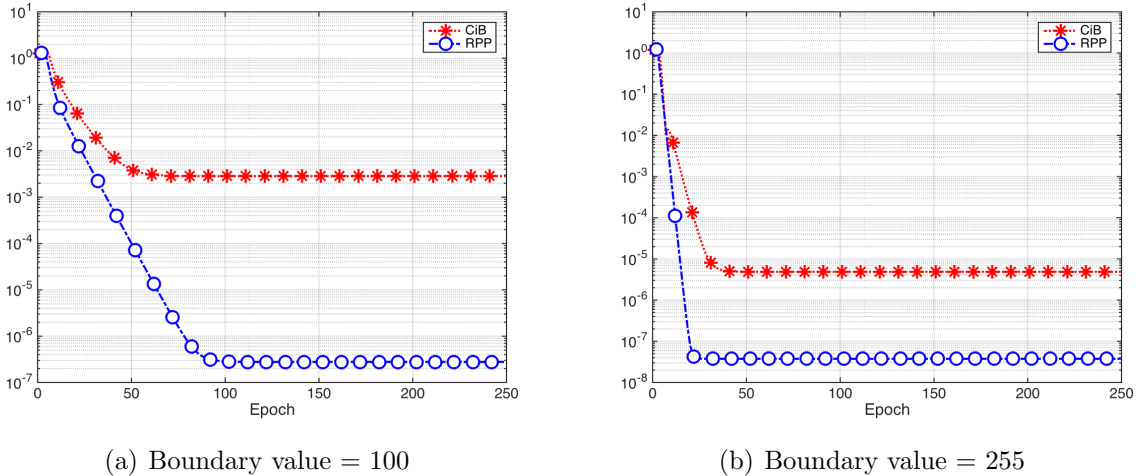


FIGURE 9. RE with PPC(-0.5, 0.5, $\frac{1}{2}$) and the boundary value (a) 100 and (b) 255

We also use the less tolerant stopping rule

$$\frac{\| |A_k A_k^\dagger u_k^l| - b \| - \| |A_k A_k^\dagger u_k^{l+1}| - b \|}{\| |A_k A_k^\dagger u_k^l| - b \|} \leq 10^{-5}$$

for the inner loops with the maximum number of iteration capped at 80, the rate of convergence accelerates.

Fig. 9 demonstrates the capability of the bright-field boundary condition to eliminate the linear phase ambiguity as the stronger error metric (88) decays geometrically before settling down to the final level of accuracy. The higher boundary value (255 in Fig. 9(a)) leads to faster convergence than the lower boundary value (100 in Fig. 9(b)). The final level of accuracy, however, depends on how accurately the inner loops for each epoch are solved. For example, increasing the maximum number of iteration from 80 to 110, significantly enhances the final accuracy of reconstruction (not shown).

The capability of removing the linear phase ambiguity is particularly important for 3D blind tomography as the different linear phase ramps for different projections would collectively create enormous 3D ambiguities that are difficult to make consistent.

9.8. Comparison with rPIE. In this section, we compare the performance of DRSAM in Fig. 9 (a) with that of the regularized PIE (rPIE) [31], the most up-to-date version of ptychographic iterative engine (PIE).

Instead of using all the 64 diffraction patterns simultaneously to update the object and probe estimates, rPIE uses one diffraction pattern at a time in a random order. As such rPIE is analogous to minibatch gradient descent in machine learning. The potential benefits include efficient memory use and a good speed boost by parallel computing resources. Unfortunately, rPIE often fail to converge in the current setting.

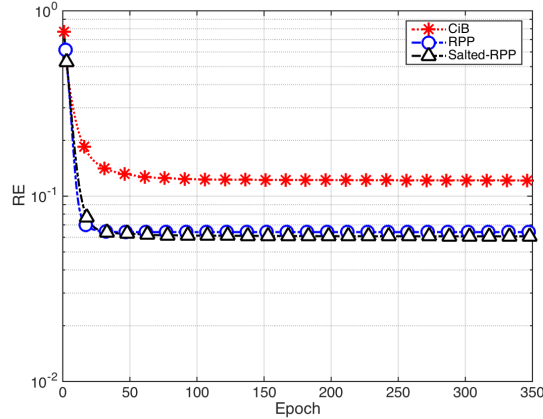


FIGURE 10. rPIE reconstruction of various objects (CiB, RPP, salted RPP) with the probe initialization PPC $(0, 0, \frac{1}{40})$. The salted RPP is created by adding impulse noise to RPP.

To obtain reasonable results, we make two adjustments. First, we reduce the phase range of RPP from $(-\pi, \pi]$ to $(-\pi/2, \pi/2)$. Second, we use PPC $(0, 0, \frac{1}{40})$ for the probe initialization.

There are three adjustable parameters in rPIE and we select these values $\alpha = 0.95, \gamma_{\text{prb}} = 0.95, \gamma_{\text{obj}} = 0.9$ (see [31] for definition). The order of updating small patches is randomly shuffled in each experiment. For each test image, we run 20 independent experiments and present the best run in Fig. 10.

10. CONCLUSION

We have presented phase retrieval algorithms based on Douglas-Rachford Splitting, which are based on the proximal relaxation of the classical Douglas-Rachford algorithm with the relaxation parameter ρ .

We have proved that for $\rho \geq 1$ all linearly stable fixed points must be regular solutions (Theorem 5.2) and that for $\rho \geq 0$ all regular solutions are linearly stable (Theorem 5.3). In other words, for $\rho \geq 1$, we need not concern with the problem of stagnation near a non-solutional fixed point which is a common problem with alternating projections. We have also proved that the regular solutions are strictly attractive under additional general conditions (Corollary 6.2). On the other hand, the problem of divergence (associated with CDR) when the data constraint is infeasible (inconsistent) does not arise in view of Theorem 4.6.

A main contribution is the selection of an optimal step size ($\rho = 1$) based on the fixed point and stability analysis and the formation of the simple, efficient algorithm (Gaussian DRS) without any tuning parameter that takes the form of Averaged Projection-Reflection.

When applied to blind ptychography, our algorithms converge geometrically from the PPC initialization informed by uniqueness theory in [16].

APPENDIX A. MEASUREMENT MATRICES

Let $\mathbb{Z}_n^2 = \llbracket 0, n-1 \rrbracket^2$ be the object domain containing the support of the discrete object f where $\llbracket k, l \rrbracket$ denotes the integers between, and including, $k \leq l \in \mathbb{Z}$. Let $\mathcal{M}^0 := \mathbb{Z}_m^2, m < n$, be the initial probe area, i.e. the support of the probe μ^0 describing the illumination field.

Let \mathcal{T} be the set of all shifts, including $(0, 0)$, involved in the ptychographic measurement. Denote by $\mu^{\mathbf{t}}$ the \mathbf{t} -shifted probe for all $\mathbf{t} \in \mathcal{T}$ and $\mathcal{M}^{\mathbf{t}}$ the domain of $\mu^{\mathbf{t}}$. Let $f^{\mathbf{t}}$ the object restricted to $\mathcal{M}^{\mathbf{t}}$. We refer to each $f^{\mathbf{t}}$ as a part of f and write $f = \vee_{\mathbf{t}} f^{\mathbf{t}}$ where \vee is the ‘‘union’’ of functions consistent over their common support set. In ptychography, the original object is broken up into a set of overlapping object parts, each of which produces a $\mu^{\mathbf{t}}$ -coded diffraction pattern. The totality of the coded diffraction patterns is called the ptychographic measurement data. For convenience, we assume the value zero for $\mu^{\mathbf{t}}, f^{\mathbf{t}}$ outside of $\mathcal{M}^{\mathbf{t}}$ and the periodic boundary condition on \mathbb{Z}_n^2 when $\mu^{\mathbf{t}}$ crosses over the boundary of \mathbb{Z}_n^2 .

Let the μ -Fourier transform of f^0 be written as

$$F^0(\mathbf{w}) = \sum_{\mathbf{k} \in \mathcal{M}^0} e^{-i2\pi\mathbf{k} \cdot \mathbf{w}} \mu^0(\mathbf{k}) f^0(\mathbf{k}), \quad \mathbf{w} = (w_1, w_2) \in [0, 1]^2.$$

and the μ -coded diffraction pattern as

$$(89) \quad |F^0(\mathbf{w})|^2 = \sum_{\mathbf{k} \in \widetilde{\mathcal{M}}^0} \left\{ \sum_{\mathbf{k}' \in \mathcal{M}^0} \mu^0(\mathbf{k} + \mathbf{k}') f^0(\mathbf{k}' + \mathbf{k}) \overline{\mu^0(\mathbf{k}') f^0(\mathbf{k}')} \right\} e^{-i2\pi\mathbf{k} \cdot \mathbf{w}}$$

where

$$\widetilde{\mathcal{M}}^0 = \{(k_1, k_2) \in \mathbb{Z}^2 : -m + 1 \leq k_1 \leq m - 1, -m + 1 \leq k_2 \leq m - 1\}.$$

Here and below the over-line notation means complex conjugacy. In view of (90), we sample the coded diffraction pattern on the grid

$$(90) \quad L = \left\{ (w_1, w_2) \mid w_j = 0, \frac{1}{2m-1}, \frac{2}{2m-1}, \dots, \frac{2m-2}{2m-1} \right\}.$$

We assume randomness in the phases θ of the mask function $\mu^0(\mathbf{n}) = |\mu^0(\mathbf{n})| e^{i\theta(\mathbf{n})}$ where $\theta(\mathbf{n})$ are independent, continuous real-valued random variables over $[0, 2\pi)$. We also require that $|\mu^0(\mathbf{n})| \neq 0, \forall \mathbf{n} \in \mathcal{M}^0$.

Let $\mathcal{F}(\nu^0, g)$ be the bilinear transformation representing the totality of the Fourier (magnitude and phase) data for any probe ν and object g . From $\mathcal{F}(\nu^0, g)$ we can define two measurement matrices. First, for a given $\nu^0 \in \mathbb{C}^{m^2}$, let A_ν be defined via the relation $A_\nu g := \mathcal{F}(\nu^0, g)$ for all $g \in \mathbb{C}^{n^2}$; second, for a given $g \in \mathbb{C}^{n^2}$, let B_g be defined via $B_g \nu = \mathcal{F}(\nu^0, g)$ for all $\nu^0 \in \mathbb{C}^{m^2}$.

More specifically, let Φ denote the L -sampled Fourier matrix. The measurement matrix A_ν is a concatenation of $\{\Phi \text{diag}(\nu^{\mathbf{t}}) : \mathbf{t} \in \mathcal{T}\}$ (Figure (11)(a)). Likewise, B_g is $\{\Phi \text{diag}(g^{\mathbf{t}}) : \mathbf{t} \in \mathcal{T}\}$ stacked on top of each other (Figure (11)(b)).

The most relevant feature of the measurement matrices to the present work is that both $A_\nu A_\nu^\dagger$ and $B_g B_g^\dagger$ are *orthogonal* projections.

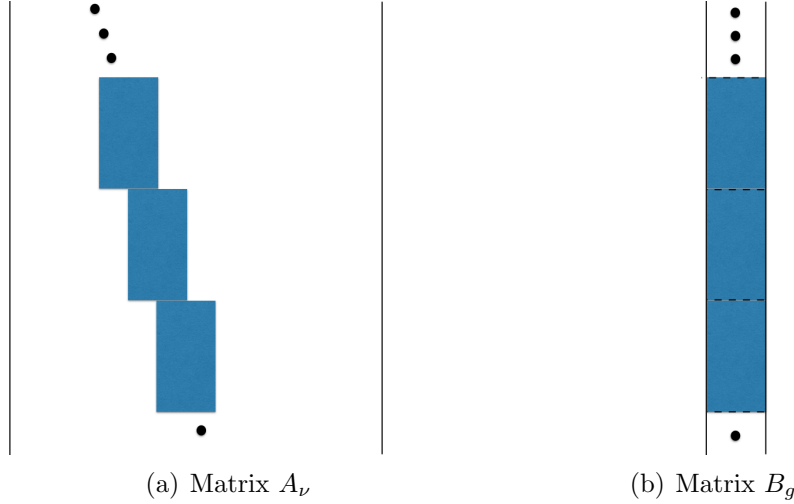


FIGURE 11. (a) A_ν is a concatenation of shifted blocks $\{\Phi \text{diag}(\nu^{\mathbf{t}}) : \mathbf{t} \in \mathcal{T}\}$; (b) B_g is a concatenation of unshifted blocks $\{\Phi \text{diag}(g^{\mathbf{t}}) : \mathbf{t} \in \mathcal{T}\}$. In both cases, each block gives rise to a coded diffraction pattern $|\Phi(\nu^{\mathbf{t}} \odot g^{\mathbf{t}})|$.

Since Φ has orthogonal columns, both A_ν and B_g have orthogonal columns. By proper normalization, we can write both A_ν and B_g in the form ΨD where Ψ is an isometry and D is a diagonal matrix. As a result, both $A_\nu A_\nu^\dagger$ and $B_g B_g^\dagger$ are Hermitian symmetric and hence define *orthogonal* projections for any ν and g .

We simplify the notation by setting $A = A_\mu$ and $B = B_f$.

APPENDIX B. THE POISSON VERSUS GAUSSIAN LOG-LIKELIHOOD FUNCTIONS

Poisson distribution

$$P(n) = \frac{\lambda^n e^{-\lambda}}{n!}$$

Let $n = \lambda(1 + \epsilon)$ where $\lambda \gg 1$ and $\epsilon \ll 1$. Using Stirling's formula

$$n! \sim \sqrt{2\pi n} e^{-n} n^n$$

in the Poisson distribution, we obtain

$$\begin{aligned} P(n) &\sim \frac{\lambda^{\lambda(1+\epsilon)} e^{-\lambda}}{\sqrt{2\pi} e^{-\lambda(1+\epsilon)} [\lambda(1+\epsilon)]^{\lambda(1+\epsilon)+1/2}} \\ &\sim \frac{1}{\sqrt{2\pi\lambda} e^{-\lambda\epsilon} (1+\epsilon)^{\lambda(1+\epsilon)+1/2}}. \end{aligned}$$

By the asymptotic

$$(1 + \epsilon)^{\lambda(1+\epsilon)+1/2} \sim e^{\lambda\epsilon + \lambda\epsilon^2/2}$$

we have

$$(91) \quad P(n) \sim \frac{e^{-\lambda\epsilon^2/2}}{\sqrt{2\pi\lambda}} = \frac{e^{-(n-\lambda)^2/(2\lambda)}}{\sqrt{2\pi\lambda}}.$$

Namely in the low noise limit the Poisson noise is equivalent to the Gaussian noise of the mean $|Af|^2$ and the variance equal to the intensity of the diffraction pattern. The overall SNR can be tuned by varying the signal energy $\|Af\|^2$.

The negative log-likelihood function for the right hand side of (91) is

$$(92) \quad \sum_j \ln |u[j]| + \frac{1}{2} \left| \frac{b[j]}{|u[j]|} - |u[j]| \right|^2, \quad b = \text{noisy diffraction pattern.}$$

For small NSR and in the vicinity of b , we make the substitution

$$\frac{\sqrt{b[j]}}{|u[j]|} \rightarrow 1, \quad \ln |u[j]| \rightarrow \ln \sqrt{b[j]}$$

to obtain

$$(93) \quad \text{const.} + \frac{1}{2} \sum_j \left| \sqrt{b[j]} - |u[j]| \right|^2.$$

APPENDIX C. PERTURBATION ANALYSIS OF THE POISSON DRS

The full analysis of the Poisson DRS (23) is more challenging. Instead, we give a perturbative derivation of analogous result to Theorem 4.6 for the Poisson DRS with small positive ρ .

For small ρ , by keeping only the terms up to $\mathcal{O}(\rho)$ we obtain the perturbed DRS:

$$(94) \quad u_{k+1} = \frac{1}{2}u_k - \frac{1}{2}\left(1 - \frac{\rho}{2}\right)x_k + P_Y x_k$$

where $x_k = R_X u_k$.

Writing

$$I = P_X + P_X^\perp \quad \text{and} \quad R_X = P_X - P_X^\perp,$$

we then have the estimates

$$\begin{aligned} \|u_{k+1}\| &\leq \left\| \frac{\rho}{4}P_X u_k + \left(1 - \frac{\rho}{4}\right)P_X^\perp u_k \right\| + \|P_Y x_k\| \\ &\leq \left(1 - \frac{\rho}{4}\right)\|u_k\| + \|b\| \end{aligned}$$

since ρ is small. Iterating this bound, we obtain

$$\|u_{k+1}\| \leq \left(1 - \frac{\rho}{4}\right)^k \|u_1\| + \|b\| \sum_{j=0}^{k-1} \left(1 - \frac{\rho}{4}\right)^j$$

and hence

$$(95) \quad \limsup_{k \rightarrow \infty} \|u_k\| \leq \frac{4}{\rho} \|b\|.$$

Note that the small ρ limit and the Poisson-to-Gaussian limit in Appendix B do not commute, resulting in a different constant in (95) from Theorem 4.6.

APPENDIX D. EIGEN-STRUCTURE

The vector space $\mathbb{C}^N = \mathbb{R}^N \oplus_{\mathbb{R}} i\mathbb{R}^N$ is isomorphic to \mathbb{R}^{2N} via the map

$$G(v) := \begin{bmatrix} \Re(v) \\ \Im(v) \end{bmatrix}, \quad \forall v \in \mathbb{C}^N$$

and endowed with the real inner product

$$\langle u, v \rangle := \Re(u^*v) = G(u)^\top G(v), \quad u, v \in \mathbb{C}^N.$$

We say u and v are orthogonal to each other (denoted by $u \perp v$) iff $\langle u, v \rangle = 0$.

Let $\lambda_1 \geq \lambda_2 \geq \dots \geq \lambda_{2n} \geq \lambda_{2n+1} = \dots = \lambda_N = 0$ be the singular values of \mathcal{H} with the corresponding right singular vectors $\{\eta_k \in \mathbb{R}^N\}_{k=1}^N$ and left singular vectors $\{\xi_k \in \mathbb{R}^{2n}\}_{k=1}^{2n}$. By definition, for $k = 1, \dots, 2n$,

$$(96) \quad H^* \eta_k = \lambda_k G^{-1}(\xi_k),$$

$$(97) \quad \Re[HG^{-1}(\xi_k)] = \lambda_k \eta_k.$$

Proposition D.1. *We have $\xi_1 = G(f)$, $\xi_{2n^2} = G(-if)$, $\lambda_1 = 1$, $\lambda_{2n^2} = 0$ as well as $\eta_1 = |Af|$.*

Proof. Since

$$Hf = \Omega_0^* A_\infty f = |Af|$$

we have by (68)

$$(98) \quad \Re[Hf] = \mathcal{H}^\top \xi_1 = |Af|, \quad \Im[Hf] = \mathcal{H}^\top \xi_{2n^2} = 0$$

and hence the results. □

Corollary D.2.

$$(99) \quad \begin{aligned} \lambda_2 &= \max\{\|\Im(Hu)\| : u \in \mathbb{C}^n, u \perp if, \|u\| = 1\} \\ &= \max\{\|\mathcal{H}^\top u\| : u \in \mathbb{R}^{2n^2}, u \perp \xi_1, \|u\| = 1\} \end{aligned}$$

Proof. By (68),

$$\Im[Hu] = \mathcal{H}^\top G(-iu).$$

The orthogonality condition $iu \perp f$ is equivalent to

$$G(x_0) \perp G(-iu).$$

Hence, by Proposition D.1 ξ_2 is the maximizer of the right hand side of (99), yielding the desired value λ_2 . □

Proposition D.3. *For $k = 1, \dots, 2n^2$,*

$$(100) \quad \lambda_k^2 + \lambda_{2n^2+1-k}^2 = 1$$

$$(101) \quad \xi_{2n^2+1-k} = G(-iG^{-1}(\xi_k))$$

$$(102) \quad \xi_k = G(iG^{-1}(\xi_{2n^2+1-k})).$$

Proof. Since H is an isometry, we have $\|w\| = \|Hw\|, \forall w \in \mathbb{C}^n$. On the other hand, we have

$$\|Hw\|^2 = \|G(Hw)\|^2 = \|\mathcal{H}^\top G(w)\|^2 + \|\mathcal{H}^\top G(-iw)\|^2$$

and hence

$$(103) \quad \|G(w)\|^2 = \|\mathcal{H}^\top G(w)\|^2 + \|\mathcal{H}^\top G(-iw)\|^2.$$

Now we prove (100), (101) and (102) by induction.

Recall the variational characterization of the singular values/vectors

$$(104) \quad \lambda_j = \max_{\|u\|=1} \|\mathcal{H}^\top u\|, \quad \xi_j = \arg \max_{\|u\|=1} \|\mathcal{H}^\top u\|, \quad \text{s.t. } u \perp \xi_1, \dots, \xi_{j-1}, \quad \|u\| = 1$$

By Proposition D.1, (100), (101) and (102) hold for $k = 1$. Suppose (100), (101) and (102) hold for $k = 1, \dots, j-1$ and we now show that they also hold for $k = j$.

Hence by (103)

$$\lambda_j^2 = \max_{\|u\|=1} \|\mathcal{H}^\top u\|^2 = 1 - \min_{\|v\|=1} \|\mathcal{H}^\top v\|^2, \quad \text{s.t. } u \perp \xi_1, \dots, \xi_{j-1}, \quad v = G(-iG^{-1}(u)).$$

The condition $u \perp \xi_1, \dots, \xi_{j-1}$ implies $v \perp \xi_{2n^2}, \dots, \xi_{2n^2+2-j}$ and vice versa. By the dual variational characterization to (104)

$$\lambda_{2n^2+1-j} = \min_{\|u\|=1} \|\mathcal{H}^\top u\|, \quad \xi_{2n^2+1-j} = \arg \min_{\|u\|=1} \|\mathcal{H}^\top u\|, \quad \text{s.t. } u \perp \xi_{2n^2}, \dots, \xi_{2n^2+2-j}, \quad \|u\| = 1,$$

we have

$$\lambda_j^2 = 1 - \lambda_{2n^2+1-j}^2, \quad \xi_{2n^2+1-j} = G(-iG^{-1}(\xi_j)).$$

□

Proposition D.4. For each $k = 1, \dots, 2n^2$,

$$(105) \quad HH^* \eta_k = \lambda_k (\lambda_k \eta_k + i \lambda_{2n^2+1-k} \eta_{2n^2+1-k}),$$

$$(106) \quad HH^* \eta_{2n^2+1-k} = \lambda_{2n^2+1-k} (\lambda_{2n^2+1-k} \eta_{2n^2+1-k} - i \lambda_k \eta_k).$$

Proof. By definition, $\mathcal{H} \eta_k = \lambda_k \xi_k$. Hence

$$H^* \eta_k = (\Re[H^*] + i \Im[H^*]) \eta_k = \lambda_k (\xi_k^R + i \xi_k^I)$$

where

$$\xi_k = \begin{bmatrix} \xi_k^R \\ \xi_k^I \\ \xi_k^I \\ \xi_k^R \end{bmatrix}, \quad \xi_k^R, \xi_k^I \in \mathbb{R}^n.$$

On the other hand, $\mathcal{H}^\top \xi_k = \lambda_k \eta_k$ and hence

$$(107) \quad \Re[H] \xi_k^R - \Im[H] \xi_k^I = \lambda_k \eta_k.$$

Now we compute $HH^* \eta_k$ as follows.

$$(108) \quad \begin{aligned} HH^* \eta_k &= \lambda_k H (\xi_k^R + i \xi_k^I) \\ &= \lambda_k (\Re[H] + i \Im[H]) (\xi_k^R + i \xi_k^I) \\ &= \lambda_k (\Re[H] \xi_k^R - \Im[H] \xi_k^I) + i \lambda_k (\Re[H] \xi_k^I + \Im[H] \xi_k^R) \\ &= \lambda_k^2 \eta_k + i \lambda_k (\Re[H] \xi_k^I + \Im[H] \xi_k^R) \end{aligned}$$

by (107).

Notice that

$$\begin{aligned}
\Re(H)\xi_k^I + \Im(H)\xi_k^R &= \mathcal{H}^\top \begin{bmatrix} \Re(-iG^{-1}(\xi_k)) \\ \Im(-iG^{-1}(\xi_k)) \end{bmatrix} \\
&= \mathcal{H}^\top G(-iG^{-1}(\xi_k)) \\
&= \mathcal{H}^\top \xi_{2n^2+1-k} \\
(109) \qquad \qquad \qquad &= \lambda_{2n^2+1-k} \eta_{2n^2+1-k}
\end{aligned}$$

by Proposition D.3.

Putting (108) and (109) together, we have (105). (106) follows from a similar calculation. \square

Corollary D.5. *For $k = 1, 2, \dots, 2n^2$, J_A leaves invariant the subspace $\text{span}_{\mathbb{R}}\{\eta_k, i\eta_{2n^2+1-k}\}$ and has the 2×2 matrix representation*

$$(110) \quad J_A = \lambda_{2n^2+1-k} \begin{bmatrix} \cos \theta_k & \sin \theta_k \\ -\sin \theta_k & \cos \theta_k \end{bmatrix}, \quad \lambda_{2n^2+1-k} := \cos \theta_k, \quad \lambda_k := \sin \theta_k$$

in the basis of $\{\eta_k, i\eta_{2n^2+1-k}\}$. In particular,

$$(111) \quad J_A \eta_1 = 0, \quad J_A i\eta_1 = i\eta_1$$

$$(112) \quad J_A \eta_{2n^2} = \eta_{2n^2}, \quad J_A i\eta_{2n^2} = 0.$$

where $\eta_1 = |Af|$.

Proof. By Proposition D.4, the span of η_k and $i\eta_{2n^2+1-k}$ is invariant under B^*B and hence under J_A for $k = 1, \dots, 2n^2$. Moreover, (105) and (106) imply

$$HH^* = \begin{bmatrix} \lambda_k^2 & \lambda_k \lambda_{2n^2+1-k} \\ \lambda_k \lambda_{2n^2+1-k} & \lambda_{2n^2+1-k}^2 \end{bmatrix}$$

in the basis of $\eta_k, i\eta_{2n^2+1-k}$. Hence by the definition (24) and Proposition D.3,

$$J_A = \lambda_{2n^2+1-k} \begin{bmatrix} \lambda_{2n^2+1-k} & \lambda_k \\ -\lambda_k & \lambda_{2n^2+1-k} \end{bmatrix} = \lambda_{2n^2+1-k} \begin{bmatrix} \cos \theta_k & \sin \theta_k \\ -\sin \theta_k & \cos \theta_k \end{bmatrix}, \quad \theta_k \in \mathbb{R}.$$

Hence $\lambda_{2n^2+1-k}(\lambda_{2n^2+1-k} \pm i\lambda_k)$ are eigenvalues of J_A . \square

ACKNOWLEDGEMENTS

The research of A.F. is supported by the US National Science Foundation grant DMS-1413373. A.F. thanks National Center for Theoretical Sciences (NCTS), Taiwan, where the present work was carried out, for the hospitality during his visits in June and August 2018.

REFERENCES

- [1] H.H. Bauschke, P.L. Combettes and D. R. Luke, Phase retrieval, error reduction algorithm, and Fienup variants: a view from convex optimization, *J. Opt. Soc. Am. A* **19**, 13341-1345 (2002).
- [2] H.H. Bauschke, P.L. Combettes and D. R. Luke, Hybrid projection-reflection method for phase retrieval, *J. Opt. Soc. Am. A* **20**, 1025-1034 (2003).
- [3] H. H. Bauschke, P. L. Combettes and D. R. Luke, "Finding best approximation pairs relative to two closed convex sets in Hilbert space", *J. Approx. Theory* **127** (2004) 178-192.
- [4] L. Bian, J. Suo, J. Chung, X. Ou, C. Yang, F. Chen, and Q. Dai, "Fourier ptychographic reconstruction using Poisson maximum likelihood and truncated Wirtinger gradient," *Sci. Rep.* **6** (2016), 27384.
- [5] H. H. Bauschke and J. M. Borwein, "On projection algorithms for solving convex feasibility problems", *SIAM Rev.* **38** (1996) 367-426.
- [6] O. Bunk, M. Dierolf, S. Kynde, I. Johnson, O. Marti, F. Pfeiffer, "Influence of the overlap parameter on the convergence of the ptychographical iterative engine," *Ultramicroscopy* **108** (5) (2008) 481-487.
- [7] H. Chang, P. Enfedaque and S. Marchesini, "Blind ptychographic phase retrieval via convergent alternating direction method of multipliers," *SIAM J. Imaging Sci.* **12** (2019) 153-185.
- [8] P. Chen and A. Fannjiang, "Phase retrieval with a single mask by Douglas-Rachford algorithms," *Appl. Comput. Harmon. Anal.* **44** (2018), 665-699.
- [9] P. Chen and A. Fannjiang, "Coded-aperture ptychography: uniqueness and reconstruction", *Inverse Problems* **34** (2018) 025003.
- [10] P. Chen, A. Fannjiang and G. Liu, "Phase retrieval with one or two coded diffraction patterns by alternating projection with the null initialization," *J. Fourier Anal. Appl.* **24** (2018), 719-758.
- [11] M. Dierolf, A. Menzel, P. Thibault, P. Schneider, C. M. Kewish, R. Wepf, O. Bunk, and F. Pfeiffer, "Ptychographic x-ray computed tomography at the nanoscale," *Nature* **467** (2010), 436-439.
- [12] J. Douglas and H.H. Rachford, "On the numerical solution of heat conduction problems in two and three space variables," *Trans. Am. Math. Soc.* **82** (1956), 421-439.
- [13] V. Elser, "Phase retrieval by iterated projections," *J. Opt. Soc. Am. A* **20** (2003), 40-55.
- [14] J. Eckstein and D.P. Bertsekas, "On the Douglas-Rachford splitting method and the proximal point algorithm for maximal monotone operators," *Math. Program. A* **55** (1992), 293-318.
- [15] A. Fannjiang, "Raster grid pathology and the cure," *Multiscale Model. Simul.*, to appear; arXiv:1810.00852.
- [16] A. Fannjiang & P. Chen, "Blind ptychography: uniqueness and ambiguities," arXiv:1806.02674.
- [17] A. Fannjiang and W. Liao, "Fourier phasing with phase-uncertain mask," *Inverse Problems* **29** (2013) 125001.
- [18] A. Fannjiang and Z. Zhang, "Blind ptychography by Douglas-Rachford splitting," arxiv:1809.00962.
- [19] H.M.L. Faulkner and J.M. Rodenburg, "Movable aperture lensless transmission microscopy: A novel phase retrieval algorithm," *Phys. Rev. Lett.* **93** (2004), 023903.
- [20] H.M.L. Faulkner and J.M. Rodenburg, "Error tolerance of an iterative phase retrieval algorithm for moveable illumination microscopy," *Ultramicroscopy* **103:2** (2005), 153-164.
- [21] Fienup, J. R. 1982 Phase retrieval algorithms—a comparison. *Appl. Opt.* **21**, 2758-2769.
- [22] D. Gabay and B. Mercier. A dual algorithm for the solution of nonlinear variational problems via finite element approximation. *Computers & Mathematics with Applications* **2(1)** (1976), 17-40.
- [23] P. Giselsson and S. Boyd, "Linear convergence and metric selection for Douglas-Rachford Splitting and ADMM," *IEEE Trans. Auto. Control* **62:2**(2017) 532-544.
- [24] R. Glowinski and A. Marroco. "Sur l'approximation, par éléments finis d'ordre un, et la résolution, par pénalisation-dualité d'une classe de problèmes de dirichlet non linéaires," *ESAIM: Mathematical Modelling and Numerical Analysis*, **9**(1975), 41-76.
- [25] P. Godard, M. Allain, V. Chamard, and J. Rodenburg, "Noise models for low counting rate coherent diffraction imaging," *Opt. Express* **20** (2012), 25914-25934.
- [26] R. Hesse, D. R. Luke, S. Sabach, and M.K. Tam, "Proximal heterogeneous block implicit-explicit method and application to blind ptychographic diffraction imaging," *SIAM J. Imag. Sci.* **8** (2015) pp. 426-457.

- [27] A.P. Konijnenberg, W.M.J. Coene and H.P. Urbach, “Model-independent noise-robust extension of ptychography,” *Opt. Exp.***26** (2018) 5857-5874.
- [28] C. Kuang, Y. Ma, R. Zhou, J. Lee, G. Barbastathis, R. R. Dasari, Z. Yaqoob & P.T.C. So, “Digital micromirror device-based laser-illumination Fourier ptychographic microscopy,” *Opt. Exp.* **23**(2015), 26999-27010.
- [29] G. Li & T. K. Pong, “Douglas-Rachford splitting for nonconvex optimization with application to nonconvex feasibility problems,” *Math. Program.* **A 159** (2016), 371-401
- [30] P.-L. Lions and B. Mercier, “Splitting algorithms for the sum of two nonlinear operators,” *SIAM J. Num. Anal.* **16** (1979), 964-979.
- [31] A. M. Maiden, D. Johnson and P. Li, “Further improvements to the ptychographical iterative engine,” *Optica* **4** (2017), 736-745.
- [32] A.M. Maiden, G.R. Morrison, B. Kaulich, A. Gianoncelli & J.M. Rodenburg, “Soft X-ray spectromicroscopy using ptychography with randomly phased illumination,” *Nat. Commun.* **4** (2013), 1669.
- [33] A.M. Maiden & J.M. Rodenburg, “An improved ptychographical phase retrieval algorithm for diffractive imaging,” *Ultramicroscopy* **109** (2009), 1256-1262.
- [34] G.R. Morrison, F. Zhang, A. Gianoncelli and I.K. Robinson, “X-ray ptychography using randomized zone plates,” *Opt. Exp.* **26** (2018) 14915-14927.
- [35] Y. S. G. Nashed, D. J. Vine, T. Peterka, J. Deng, R. Ross and C. Jacobsen, “Parallel ptychographic reconstruction,” *Opt. Express* **22** (2014) 32082-32097.
- [36] K.A. Nugent, “Coherent methods in the X-ray sciences,” *Adv. Phys.***59** (2010) 1-99.
- [37] X. Ou, G. Zheng and C. Yang, “Embedded pupil function recovery for Fourier ptychographic microscopy,” *Opt. Exp.* **22** (2014) 4960-4972.
- [38] X. Peng, G.J. Ruane, M.B. Quadrelli & G.A. Swartzlander, “Randomized apertures: high resolution imaging in far field,” *Opt. Express* **25** (2017) 296187.
- [39] F. Pfeiffer, “X-ray ptychography,” *Nat. Photon.* **12** (2017) 9-17.
- [40] J.M. Rodenburg and H.M.L. Faulkner, “A phase retrieval algorithm for shifting illumination”. *Appl. Phys. Lett.* **85** (2004), 4795.
- [41] M. Stockmar, P. Cloetens, I. Zanette, B. Enders, M. Dierolf, F. Pfeiffer, and P. Thibault, “Near-field ptychography: phase retrieval for inline holography using a structured illumination,” *Sci. Rep.* **3** (2013), 1927.
- [42] P. Thibault, M. Dierolf, O. Bunk, A. Menzel, F. Pfeiffer, “Probe retrieval in ptychographic coherent diffractive imaging,” *Ultramicroscopy* **109** (2009), 338-343.
- [43] P. Thibault, M. Dierolf, A. Menzel, O. Bunk, C. David, F. Pfeiffer, “High-resolution scanning X-ray diffraction microscopy”, *Science* **321** (2008), 379-382.
- [44] P. Thibault and M. Guizar-Sicairos, “Maximum-likelihood refinement for coherent diffractive imaging”. *New J. Phys.* **14** (2012), 063004.
- [45] L. Tian, Z. Liu, L-H Yeh, M. Chen, J. Zhong, L. Waller, “Computational illumination for high-speed in vitro Fourier ptychographic microscopy,” *Optica* **2** (2015) 904-911.
- [46] Z. Wen, C. Yang, X. Liu and S. Marchesini, “Alternating direction methods for classical and ptychographic phase retrieval,” *Inverse Problems* **28** (2012), 115010.
- [47] L. Yeh, J. Dong, J. Zhong, L.Tian, M. Chen, G. Tang, M. Soltanolkotabi, and L. Waller, “Experimental robustness of Fourier ptychography phase retrieval algorithms,” *Optics Express* **23** (2015) 33214-33240.
- [48] Y. Zhang, P. Song, Q. Dai, “Fourier ptychographic microscopy using a generalized Anscombe transform approximation of the mixed Poisson-Gaussian likelihood,” *Opt. Exp.* **25** (2017) 168-179.
- [49] G. Zheng, R. Horstmeyer and C. Yang, “Wide-field, high-resolution Fourier ptychographic microscopy,” *Nature Photonics* **7** (2013), 739-745.
- [50] C. Zuo, J. Sun and Q. Chen, “Adaptive step-size strategy for noise-robust Fourier ptychographic microscopy,” *Optics Express* **24** (2016), 20724-20744.

DEPARTMENT OF MATHEMATICS, UNIVERSITY OF CALIFORNIA, DAVIS, CALIFORNIA
95616, USA.